Title

Structure and noncanonical Cdk8 activation mechanism within an Argonaute-containing Mediator kinase module

Journal

Science Advances, 7(3)

ISSN

2375-2548

Authors

Li, Yi-Chuan
Chao, Ti-Chun
Kim, Hee Jong
et al.

Publication Date

2021-01-15

DOI

10.1126/sciadv.abd4484

Peer reviewed

STRUCTURAL BIOLOGY

Structure and noncanonical Cdk8 activation mechanism within an Argonaute-containing Mediator kinase module

Yi-Chuan Li[1]*, Ti-Chun Chao[1]*, Hee Jong Kim[2], Timothy Cholko[3], Shin-Fu Chen[1], Guojie Li[1], Laura Snyder[4], Kotaro Nakanishi[5], Chia-en Chang[3], Kenji Murakami[4], Benjamin A. Garcia[4,6], Thomas G. Boyer[7†], Kuang-Lei Tsai[1,8†]

The Cdk8 kinase module (CKM) in Mediator, comprising Med13, Med12, CycC, and Cdk8, regulates RNA polymerase II transcription through kinase-dependent and -independent functions. Numerous pathogenic mutations causative for neurodevelopmental disorders and cancer congregate in CKM subunits. However, the structure of the intact CKM and the mechanism by which Cdk8 is non-canonically activated and functionally affected by oncogenic CKM alterations are poorly understood. Here, we report a cryo–electron microscopy structure of *Saccharomyces cerevisiae* CKM that redefines prior CKM structural models and explains the mechanism of Med12-dependent Cdk8 activation. Med12 interacts extensively with CycC and activates Cdk8 by stabilizing its activation (T-)loop through conserved Med12 residues recurrently mutated in human tumors. Unexpectedly, Med13 has a characteristic Argonaute-like bi-lobal architecture. These findings not only provide a structural basis for understanding CKM function and pathological dysfunction, but also further impute a previously unknown regulatory mechanism of Mediator in transcriptional modulation through its Med13 Argonaute-like features.

INTRODUCTION

In eukaryotes, Mediator is a large, evolutionarily conserved, and multisubunit (25 to 30 proteins) transcriptional coactivator complex that conveys regulatory signals from activators and repressors to the RNA polymerase II (RNAPII) transcription machinery (*1*, *2*). Structurally, Mediator proteins are assembled separately into a Core Mediator (~1 MDa) and a dissociable subcomplex (~0.5 MDa), called Cdk8 kinase module (CKM) (*3*–*6*). Biochemically, Core Mediator is able to interact with the RNAPII machinery and initiate transcription (*7*, *8*), while the CKM can reversibly associate with Core Mediator to preclude RNAPII binding (*5*, *6*, *9*, *10*). The CKM was initially considered to play a repressive role in gene expression, but recent studies have shown its roles in both context-specific activation and repression of transcription (*11*, *12*).

The CKM, first identified in yeast, consists of Cdk8, CycC, Med12, and Med13 subunits (Fig. 1A) (*13*). The CycC-dependent CDK8 kinase, a colorectal cancer oncoprotein in humans (*14*), belongs to a transcriptional CDK subbranch and phosphorylates the C-terminal domain (CTD) of RNAPII Rpb1 and many transcription-associated proteins, including Transcription Factor II H (TFIIH) (*15*–*18*). Notably, CDK8 lacks a canonical phosphorylation residue within its activation segment (T-loop), and this fact, coupled with its incorporation into the large CKM complex essential for kinase activity, renders CDK8 distinct among CDK family proteins with an apparent unique and heretofore obscure activation mechanism. Human MED12, required for CDK8/CDK19 kinase activity (*6*, *19*–*21*), has been found to associate with transcriptional activators/coactivators, the REST corepressor G9a, and certain activating noncoding RNAs (*22*–*26*). However, the molecular mechanism by which MED12 activates CycC-dependent CDK8/19 remains unclear. Med13, the largest subunit in Mediator, enables association of the CKM with Core Mediator (*5*, *6*). On the basis of sequence alignment, Med13 was predicted to be a member of the PIWI protein family because of the presence of an apparent PIWI module that contains MID and PIWI [ribonuclease H (RNase H)–like] domain (*27*). The PIWI module represents a functional unit within the Argonaute (Ago)/PIWI superfamily of proteins that play crucial roles in transcriptional and posttranscriptional gene silencing (*28*). Ago proteins are further characterized by the presence of N, L1, L2, and PAZ domains, the latter of which contributes to binding of small interfering RNA/microRNA (*29*, *30*), but the previous alignment analysis identified no such domains in Med13 (*27*). Therefore, obtaining structural information of Med13 is essential to understand its functional role in Mediator-dependent transcription regulation.

Dysfunction or dysregulation of human CKM has been linked with both germline and somatic developmental and age-associated diseases. For example, mutations in MED12 are causative for several X-linked intellectual disability disorders including Opitz-Kaveggia (FG), Lujan-Fryns (Lujan), and Ohdo syndromes, and MED12 is also recurrently mutated at high frequency in uterine leiomyomas (ULs) and breast fibroadenomas, as well as prostate and other cancers (*31*–*35*). These findings suggest that delineation of the CKM structure, including resolution of its constituent subunit interactions and mechanism of CDK8 activation therein, will be essential to fully understand the function and dysfunction of Mediator-dependent transcription

[1]Department of Biochemistry and Molecular Biology, McGovern Medical School, University of Texas Health Science Center at Houston, Houston, TX, USA. [2]Biochemistry and Molecular Biophysics Graduate Group, Perelman School of Medicine, University of Pennsylvania, Philadelphia, PA, USA. [3]Department of Chemistry, University of California, Riverside, CA, USA. [4]Department of Biochemistry and Biophysics, Perelman School of Medicine, University of Pennsylvania, Philadelphia, PA, USA. [5]Department of Chemistry and Biochemistry, The Ohio State University, Columbus, OH, USA. [6]Epigenetics Institute, Perelman School of Medicine, University of Pennsylvania, Philadelphia, PA, USA. [7]Department of Molecular Medicine, University of Texas Health Science Center at San Antonio, San Antonio, TX, USA. [8]MD Anderson Cancer Center UTHealth Graduate School of Biomedical Sciences, Houston, TX, USA.
*These authors contributed equally to this work.
†Corresponding author. Email: kuang-lei.tsai@uth.tmc.edu (K.-L.T.); boyer@uthscsa.edu (T.G.B.)

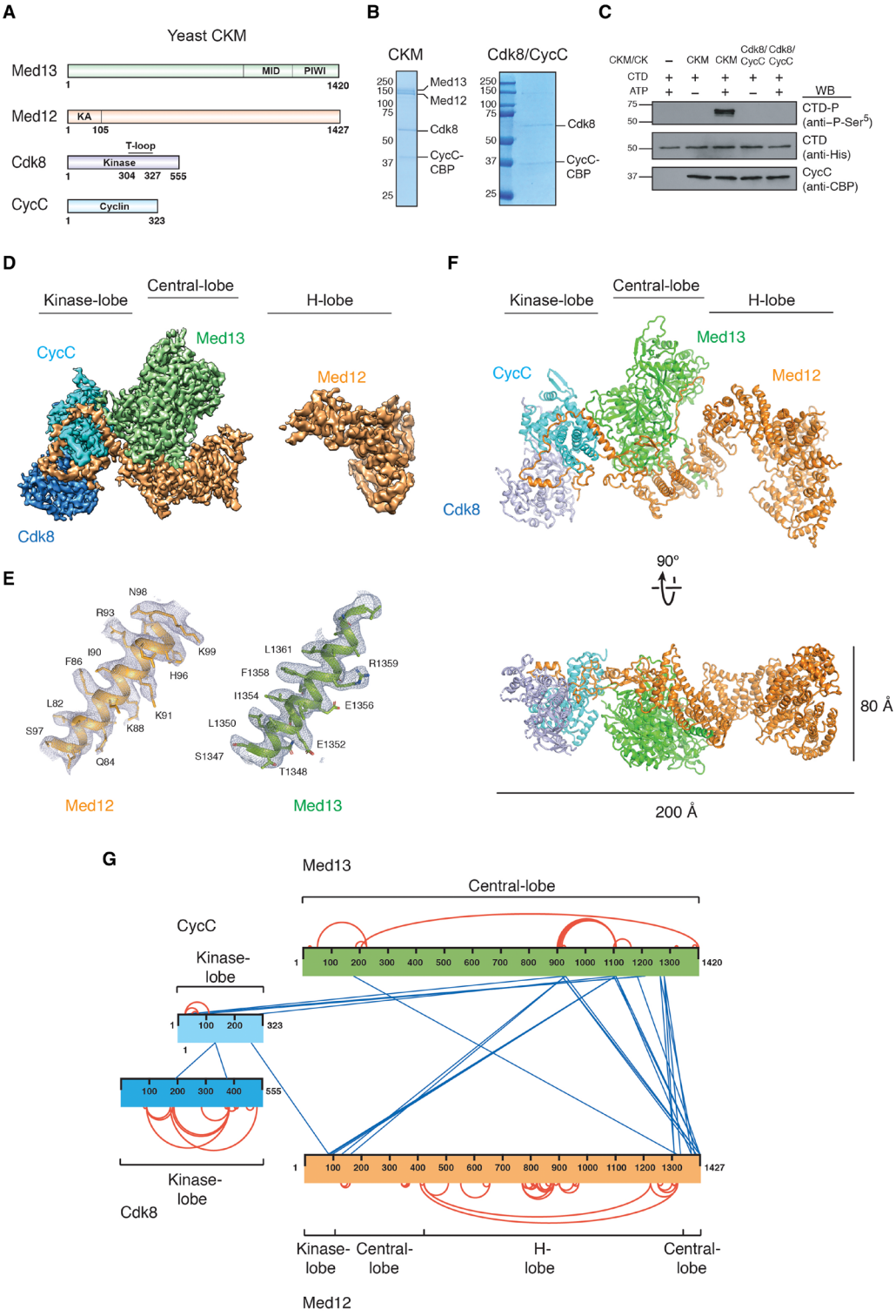

Fig. 1. Kinase activation, cryo-EM map, structure, and XL-MS analysis of the yeast CKM. (**A**) Schematic diagram of CKM subunits. The functional domains are indicated. KA, kinase activation domain. (**B**) SDS-PAGE analysis of purified WT CKM and Cdk8/CycC (from a Med12Δ/Med13Δ/CycC-TAP–tagged yeast strain). The identities of bands corresponding to Cdk8 and CycC were confirmed by MS. CBP, Calmodulin Binding Protein. (**C**) Kinase activity of purified CKM and Cdk8/CycC directed toward the Ser^5 residue of the RNAPII CTD (GST-CTD-6xHis). WB, Western blotting. (**D**) Left: Cryo-EM map of Kinase- and Central-lobes at 3.8-Å resolution. Right: Cryo-EM map of the H-lobe at 4.9-Å resolution. (Cdk8 in blue, CycC in cyan, Med13 in green, and Med12 in orange). (**E**) Two helices of Med12 and Med13 subunits with their corresponding electron densities. (**F**) Overall structure of the CKM. The Kinase-, Central-, and H-lobes are as indicated. (**G**) Cross-linking map of the CKM. In total, 80 intrasubunit and 29 intersubunit cross-links identified between lysine residues present in the CKM atomic model are shown by red and blue lines, respectively. The protein regions belonging to the Kinase-, Central-, or H-lobes are as indicated.

in development and disease. Although some structural information of human and yeast CKMs were obtained by electron microscopy (EM) and x-ray crystallography (*5*, *6*, *9*, *36*–*38*), detailed molecular insight into the entire CKM structure, subunit interactions, and mechanism of CDK8 kinase activation are heretofore still lacking.

Here, we report a cryo-EM structure of *Saccharomyces cerevisiae* CKM complex that redefines prior human and yeast CKM subunit organizational models. The structure, combined with cross-linking mass spectrometry (XL-MS) and biochemical analyses, provides a structural basis for large Med12 and Med13 subunits and reveals critical contacts between Med12 and Cdk8/CycC essential for kinase activity. The Med12 subunit functions as a scaffold within the CKM, and its unique structure provides great potential for interactions with regulators. The N-terminal region of Med12 stimulates Cdk8 kinase activity by a noncanonical mechanism that involves contacts with both the T-loop and RHYT segment of the kinase. Mapping human UL-linked MED12 driver mutations onto the CKM structure revealed a cluster in the vicinity of the kinase T-loop/RHYT segment, and functional analyses confirmed that these mutations disrupt CDK8 kinase activity. Notably, molecular dynamics simulations suggest a model for mutation-induced disruption of Cdk8 kinase activity through reconfiguration of the T-loop into a nonactivated conformation. Unexpectedly, we found that Med13 not only has MID and PIWI domains, as previously predicted, but also harbors N, L1, L2, and PAZ domains that collectively conform to an Ago structure. Notably, the L2 domain of Med13 adopts a unique structure that mimics Ago-bound RNA to occupy the central channel, resulting in an autoinhibited state. Last, we show that the CKM binding region on Core Mediator is likely to overlap with those of both RNAPII and TFIIH, revealing steric hindrance as the basis by which the CKM precludes the interaction of Mediator with the transcription preinitiation complex (PIC). Together, our findings markedly redefine the central architecture of the Mediator kinase module, confirm the interface between CDK8/CycC and MED12 as a potential therapeutic target for Mediator-associated Cdk8-driven diseases, and shed new light on the regulatory potential of Mediator in transcriptional modulation mediated by its Med13 Ago-like features.

RESULTS

High-resolution structure of the CKM redefines previous subunit organization

Wild-type (WT) yeast CKM for structure determination was purified from *S. cerevisiae* through a tandem affinity purification (TAP)–tagged CycC subunit and thereafter polished by ion exchange chromatography (table S1). Purified CKM subunit composition and kinase activity were determined by SDS–polyacrylamide gel electrophoresis (SDS-PAGE) and phosphorylation assay against the RNAPII CTD, respectively (Fig. 1, B and C). To compare the activity of Cdk8/CycC with and without Med12/Med13, we also purified endogenous yeast Cdk8/CycC from Med12/Med13 deletion strains. WT CKM kinase activity was substantially higher than that of Cdk8/CycC alone, suggesting that Cdk8/CycC activity was stimulated in the presence of Med12 and Med13 (Fig. 1C).

CKM cryo-EM specimens were prepared on holey carbon grids and imaged on a 300-kV Titan Krios (FEI) microscope equipped with a K2 Summit (Gatan) direct electron detector (fig. S1A and table S2). Two-dimensional (2D) class averages showed various orientations of the CKM that was preserved in ice (fig. S1B). Although the CKM in some averages appear to be symmetric, two distal ends of the CKM are composed of different subunits. Analysis of the CKM images resulted in an overall 4.4-Å cryo-EM map (fig. S1C). A local resolution map showed that the highest-resolution portions of the map were the Kinase- and Central-lobes, whereas some mobility resulted in blurring of the H-lobe map near the distal end (fig. S1C). Image processing that focused on the Kinase- and Central-lobes was able to produce a final 3.8-Å-resolution density map (Fig. 1D, left, and fig. S1D). For the H-lobe of the CKM near the distal terminus, local refinement was able to improve the map quality to 4.9 Å, in which secondary structure elements could be resolved and the main chain could be traced (Fig. 1D, right, and fig. S1E). We performed model building for Cdk8/CycC starting from the crystal structure of human Cdk8/CycC complex (*38*) and built Med12 and Med13 models ab initio on the basis of cryo-EM maps and secondary structure prediction results (Fig. 1, E and F; fig. S2; and table S2).

In the elongated CKM structure, two bent features, corresponding to the Kinase- and H-lobes, protrude from the Central-lobe (Fig. 1F and movie S1). In the Kinase-lobe, the Cdk8 subunit is connected to the Central-lobe through CycC and a portion of Med12, which is consistent with previous structural studies (*5*, *36*). Unexpectedly, however, we found that the H-lobe of the CKM is composed only of Med12, whereas Med13 and a portion of Med12 together constitute the Central-lobe (Fig. 1F). Notably, the relative position of Med13 and Med12 in our high-resolution structure of the CKM is reversed compared to previously published EM studies (*5*, *6*, *36*), in which Med13 was instead localized to the distal terminus of the CKM. It is likely that conformational flexibility caused by the deletion of Med13 in prior low-resolution EM studies led to inaccurate interpretation of the subunit organization.

To strengthen our structural findings, we performed XL-MS analysis on the purified CKM (fig. S3, A and B, and data S1). The identified cross-links were selected on the basis of the presence of corresponding lysine residues in our atomic model and then mapped onto the CKM structure (Fig. 1G). Except for those regions missing in the corresponding density map, the organization and interactions among subunits revealed by the CKM atomic model agree with cross-links detected by XL-MS analysis (fig. S3, C to G). Consistent with our CKM structure, several cross-links identified between CycC and Med13 occur at their interface, thus revealing CycC to be positioned next to Med13 in the Central-lobe (fig. S3D). The XL-MS results that support the CKM structure are discussed separately in the following sections. Because of sequence homologies within orthologous subunits and similarities in the CKM overall shape revealed by EM, we suggest that the subunit organization of yeast CKM redefined by our high-resolution structure and XL-MS analysis can be applied to those of higher eukaryotic CKMs.

Med12 comprises a HEAT core with N- and C-terminal protrusions that extensively interact with Cdk8/CycC and Med13, respectively

The elongated conformation of Med12 spans the entire CKM and comprises two extended N- and C-terminal segments (Med12N and Med12C, respectively), connected by a large horseshoe-shaped solenoid structure (Med12HEAT) that is mainly composed of α-helical elements (Fig. 2, A and B, and fig. S4A). Med12N (residues 1 to 105) starts as an extended polypeptide with two α helices (H1 and H2) that wrap around the Kinase-lobe of the CKM (orange in Fig. 2C) and

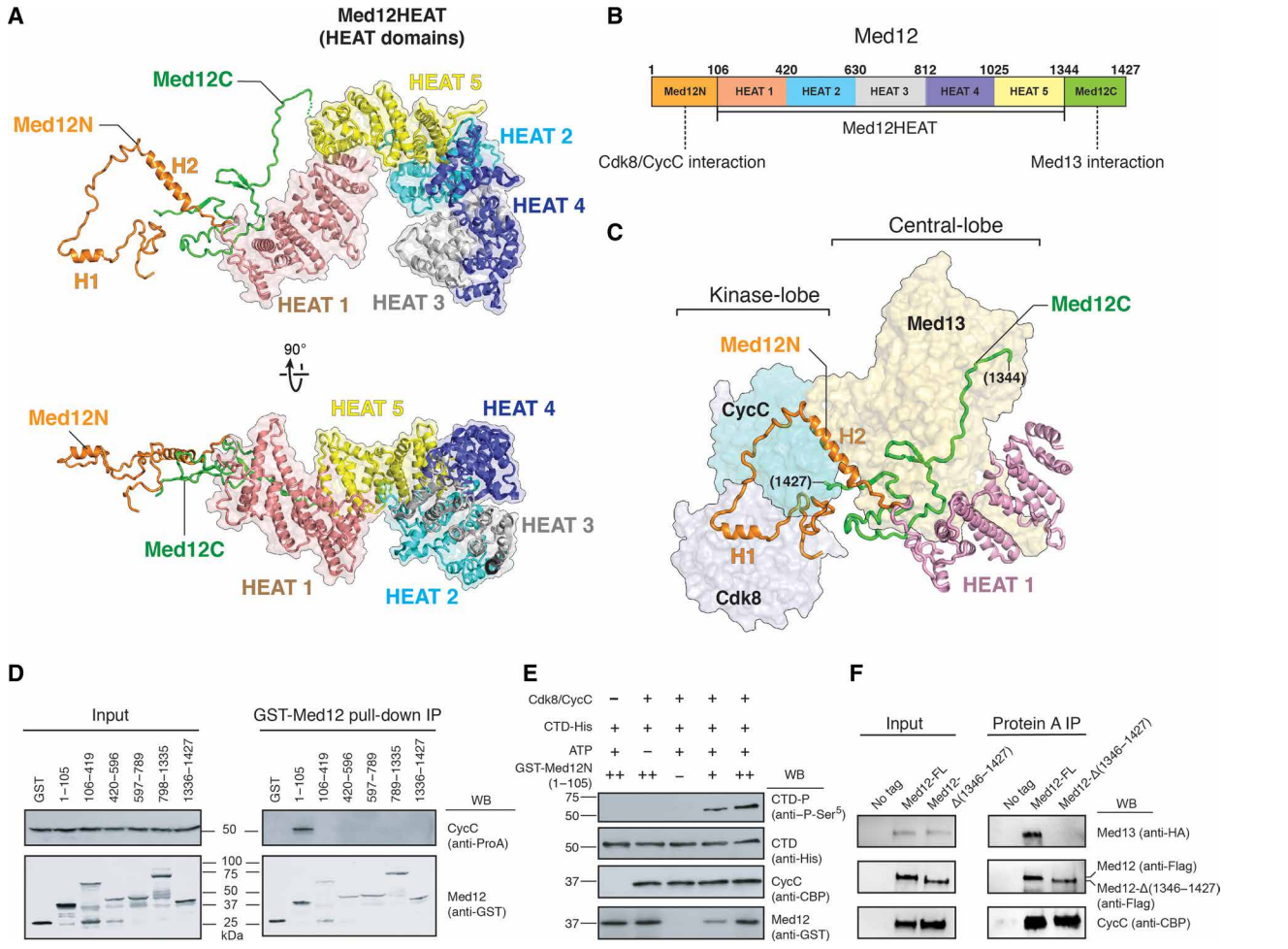

Fig. 2. Structure of Med12 and its interactions with Cdk8/CycC and Med13. (**A**) Structural organization of Med12. The first and second helices (orange ribbon) in Med12N are labeled as H1 and H2, respectively. Five HEAT domains (Med12HEAT) are shown in transparent surface. (**B**) Domain organization of Med12. The N- and C-terminal regions of Med12 (Med12N and Med12C) that form interactions with Cdk8/CycC and Med13, respectively, are indicated. Colors are as in (A). (**C**) Interactions of Med12 with Cdk8, CycC, and Med13. Cdk8, CycC, and Med13 are shown in colored surface representations. (**D**) The Med12 N-terminal region (residues 1 to 105) associates with Cdk8/CycC. GST-Med12 fragments in *Escherichia coli* lysates as indicated were immobilized on glutathione Sepharose beads and incubated with yeast cell lysate (CycC-TAP/Med12Δ/Med13Δ) containing Cdk8/CycC. (**E**) Kinase activity of yeast Cdk8/CycC stimulated by GST-Med12-(1–105). Phosphorylation of GST-CTD-6xHis was detected by the antibody that recognizes phosphorylated Ser^5 of CTD. For GST-Med12-(1–105), 250 ng (+) or 1 μg (++) of protein was used in the reactions. (**F**) Immunoprecipitation (IP) assay. Deletion of the C-terminal region (residues 1346 to 1427) of Med12 caused loss of Med13 from CKM.

makes extensive contacts with both the Cdk8 and CycC subunits (described below). This agrees with XL-MS results showing that H2 of Med12 (K88 and K91) cross-linked with CycC (K262) and Med13 (K1114) at their respective interfaces (fig. S3D). Consistent with prior biochemical findings for the human CKM (*19*, *20*), we found that the yeast Med12 N-terminal region (residues 1 to 105) could associate with Cdk8/CycC and stimulate its kinase activity (Fig. 2, D and E), confirming an important role for the Med12 N-terminal region in kinase activation. Med12HEAT (residues 106 to 1343), encompassing the majority of Med12, comprises five HEAT domains, each of which consists of 9 to 14 α helices (Fig. 2B and fig. S4B). The first domain (HEAT 1) of Med12HEAT lies adjacent to Med13 in the best-resolved portion of the cryo-EM map, and we were able to assign protein residues for this domain in the atomic model (Fig. 2C and fig. S2B). The remaining four domains (HEAT 2 to HEAT 5) of Med12HEAT, which form the H-lobe, are tightly packed at one end of the CKM (Fig. 1F and fig. S2C). Despite decreased resolution (4.9 Å) in this region caused by some mobility, the main-chain trajectory of the H-lobe revealed by our model agreed with cross-links detected by the XL-MS analysis of the CKM (fig. S3E).

In the CKM structure, we found that Med12C (residues 1344 to 1427; green in Fig. 2C) adopts an extended conformation that runs along the Med13 surface, overlaps with a linker region that connects Med12N to HEAT 1, and ultimately contacts CycC by its C terminus near the interface between Med13 and CycC (Fig. 2C and fig. S4, C to E). Consistent with the localization of the Med12 C terminus, XL-MS analysis revealed cross-links between K1392 and K1424 of Med12 and some Lys residues of Med13 around the interface between Med13 and CycC (fig. S3F). In addition, the extensive interactions between Med13 and Med12C described here are consistent with our biochemical observation that Med13 is lost from a ΔMed12C

CKM derivative (Fig. 2F). Moreover, the C-terminal region of human MED12, including both PQL and OPA domains, has been reported to interact with Med13 (*20*). Together, these results reveal that Med12 functions as a scaffold that connects Cdk8, CycC, and Med13, and its elongated conformation could further provide a large surface area for interactions with transcriptional regulators.

Structure of Cdk8/CycC within the CKM reveals a stabilized T-loop

Structural studies of CDK2/CycA established the general principle of kinase activation for the CDK family proteins (*39*). Activation occurs through the binding of the Cyclin to the CDK followed by phosphorylation of a conserved residue in the T-loop of the CDK. The phosphorylated T-loop is extended to form a platform, which relieves a blockade to the catalytic site present in free CDK, leading to fully activated kinase. Notably, among all human CDK proteins, CDK8 (and its close paralog CDK19) uniquely lacks a canonical phosphorylation residue in the T-loop, suggesting an activation mechanism distinct from the other classical CDK proteins.

Within the CKM, the structure of yeast Cdk8 reveals a bilobed architecture (N- and C-lobes) with a peptide substrate–binding site located between the two lobes (Fig. 3A and fig. S5A, left). CycC consists of two classical cyclin-box fold domains, N-CBF and C-CBF. The N-CBF in CycC is bound by the N-lobe of Cdk8, including an N-terminal helix (α1) present in Cdk8 that provides specificity for CycC recognition. A conserved groove (yellow in fig. S5A) unique to CycC (among all Cyclin family proteins) lies near the T-loop of Cdk8. The overall structures of yeast and human Cdk8/CycC are generally similar (fig. S5, A and B) (*38*). Compared to the human CDK8/CycC structure, the α1 of Cdk8 and the C-terminal helix of CycC in yeast adopt slightly different orientations due to an additional β sheet (S1 and S2) in the latter formed by an insertion of ~30 amino acids between H2 and H3 (fig. S5C). All T-loops in the structures of human CDK8/CycC alone, determined in the absence of MED12/MED13, are mostly disordered (fig. S5D), suggesting that these structures exhibit only partially active conformations. By contrast, the T-loop of yeast Cdk8 within the CKM is well defined in the electron density map (fig. S5A, right). Furthermore, when compared to the structure of human phosphorylated (activated) CDK2 (*40*), yeast Cdk8 with the CKM shares notable structural similarities in its peptide substrate–binding site. First, four highly conserved residues in yeast Cdk8 important for coordinating the T-loop in an activated conformation, including R206 (N-lobe), R285 (C-lobe), R309 (T-loop), and Y342 (RHYT segment), all adopt similar side-chain orientations as observed in the phosphorylated CDK2 (fig. S5E, left). Similarly, the side chain of Y342 forms a hydrogen bond with the side chain of R285 in Cdk8. Second, the VVT motif (V325-V326-T327) of CKM Cdk8 reveals a "push-in" conformation, similar to that of phosphorylated Cdk2, resulting in a potential substrate-binding site. Third, residues 304 to 306 next to the adenosine triphosphate (ATP)–binding site, at the start of the T-loop in CKM Cdk8, adopts a "DLG-in" (DMG motif in human CDK8) conformation crucial for kinase activity, which is similar to that of phosphorylated CDK2 (fig. S5E, left bottom). Together, these observations suggest that the T-loop of Cdk8 within the CKM is poised in an activated conformation. Because Med12 physically interacts and functionally stimulates CycC/Cdk8 within the CKM, we examined whether and how Med12 contributes to stabilization of the Cdk8 T-loop.

Med12 wraps around CycC and folds on the T-loop and RYHT segment of Cdk8

The N-terminal region of Med12 (Med12N) adopts an extended conformation that encircles the C-CBF of CycC and contacts the C-lobe of Cdk8, resulting in a total interaction area of ~3800 $Å^2$ (Fig. 3A, fig. S2D, and movie S2). We divided the overall interface between Med12N and CycC into three regions. In the first, the N-terminal coil region (I, residues 11 to 35) before H1 in Med12 contacts the C-CBF near Cdk8 and the N terminus of CycC (Fig. 3A and fig. S4F). Trp6, highly conserved in the CycC family, is buried almost completely between hydrophobic residues in this area (fig. S4G). The second interface involves a coil region (II, residues 59 to 73) followed by H2 within Med12 and the conserved surface groove on CycC that is formed between its two CBFs (Fig. 3B), including five residues (R92, Q93, W209, D214, and Y297) that are invariantly conserved among CycC, but not other Cyclin family proteins. These interactions are likely responsible for the specificity of CycC for Med12. The third interface (III) corresponds to a composite binding region involving the C-CBF of CycC and both H2 of Med12 and a linker region from Med13 (Fig. 3A and fig. S4H). Med13 contacts in this area could stabilize the interaction between Med12 and CycC, which may explain our previous biochemical observation that the presence of human MED13 could suppress dissociation of oncogenic MED12 mutant derivatives from Cdk8/CycC (*20*).

Regarding the interface between Med12 and Cdk8, the N-terminal portion of Med12 (residues 35 to 56) folds on the C-lobe of Cdk8 where it makes numerous interactions, primarily with the T-loop and the α6-α7 loop (RHYT segment) of Cdk8 (Fig. 3A). The residue W36 of Med12, together with residues W281, L283, and P344 of Cdk8, forms a hydrophobic core that buries residue F311 of the T-loop (Fig. 3C). Med12 residues E42 and L46 within H1 (residues 40 to 49) along with Med12 residues A51, K52, and G53 contact the RHYT segment. Notably, residues 54 to 56, following H1 of Med12, form some contacts with the tip of the T-loop (Fig. 3D). This interaction mode is reminiscent of the unphosphorylated CDK6/Vcyclin complex, in which the N terminus of Vcyclin forms a short β sheet with the CDK6 T-loop to activate the kinase (fig. S5F) (*41*).

To confirm the interaction mode between Med12N and Cdk8/CycC revealed by structural analysis, we assessed the impact of both interfacial and noninterfacial mutations in CycC and Cdk8 on Med12 binding using immobilized protein affinity chromatography (Fig. 3, E and F). Compared to WT Cdk8/CycC, mutant derivatives S210E or F235E in CycC or I449E in Cdk8, all of which alter residues that interface with Med12N, were severely compromised in their respective abilities to bind Med12N. As expected, mutant derivatives A251R in CycC and D410R in Cdk8 that are not involved in Med12 interaction exhibited no reduction in Med12N binding.

Med12 binds to the Cdk8 RHYT segment, leading to T-loop stabilization

Intriguingly, our structural analysis revealed that within the CKM, the Cdk8 T-loop is nonetheless configured into an activated conformation despite the fact that it lacks a canonical phosphorylation residue (fig. S5E, left). Since Med12N contacts both the T-loop and RHYT segment of Cdk8 and is important for kinase activity, we speculated that Med12 H1 supersedes the requirement for T-loop phosphorylation by configuring the T-loop into an activated conformation. To investigate this possibility, we assessed the structural features of the Cdk8 RHYT and T-loop segments in the presence and absence of

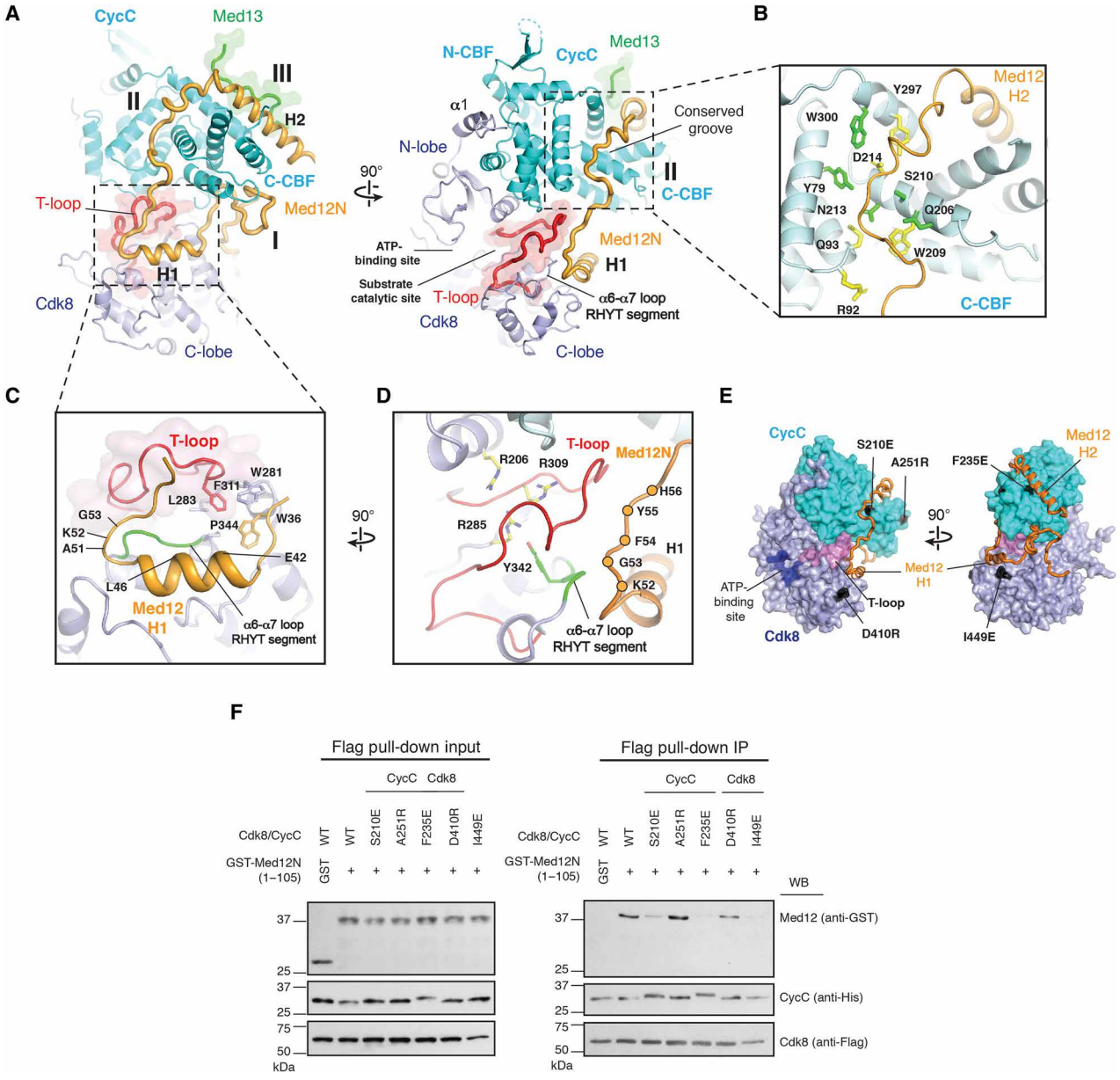

Fig. 3. Med12N bound to Cdk8/CycC. (**A**) Structure of Cdk8/CycC contacted by Med12N (orange) and a linker region of Med13 (green). The T-loop of Cdk8 is colored in red and highlighted by the red surface. The highly conserved groove within the CycC family proteins is indicated. (**B**) Contacts between Med12N and the highly conserved groove in CycC. The residues in CycC involved in Med12 binding are indicated. The highly conserved residues are colored in yellow. (**C**) Detailed view of the interface between Cdk8 (light blue) and Med12 H1 (orange). The RHYT segment is colored in green. (**D**) The residues following Med12 H1 involved in interactions with the T-loop and α6-α7 loop (RHYT segment) of Cdk8 are indicated by orange circles. Three conserved arginine (R206, R285, and R309) and one tyrosine (Y342) residues in Cdk8 important for coordinating an active T-loop conformation are shown. (**E**) Surface representation of Cdk8/CycC/Med12N showing positions of mutations. (**F**) Pull-down analysis for interaction of WT or mutant Cdk8/CycC with GST-Med12N-(1–105).

Med12. Notably, because the RHYT segment, similar to the T-loop, is conserved and present in both yeast and human Cdk8 proteins, we therefore compared the structure of yeast Cdk8 (bound by Med12 within the CKM) to that of human CDK8 (absent MED12).

In our CKM structure, the Cdk8 RHYT segment, bound by MED12 residues E42, L46, A51, K52, and G53, adopts a conformation that makes several contacts with the T-loop (Fig. 4A). Thus, Cdk8 residues R340 and Y342 from the RHYT segment contact residues Y319 (as well as residue T317) and L318, respectively, within the T-loop. Notably, the side chain of Y342 interacts with R285 (C-lobe), one of three highly conserved arginine residues in CDK family proteins important for coordinating the T-loop in an activated conformation (Fig. 4A and fig. S5E, left). By contrast, in human CDK8 structures (absent MED12), the RHYT segment adopts a different conformation and is instead positioned such that it could potentially overlap with the T-loop (Fig. 4B and fig. S5E, middle). In this regard, the side chain of Y211 (Y342 in yeast Cdk8) does not engage in hydrogen bonding with R150 (R285 in yeast Cdk8) but instead

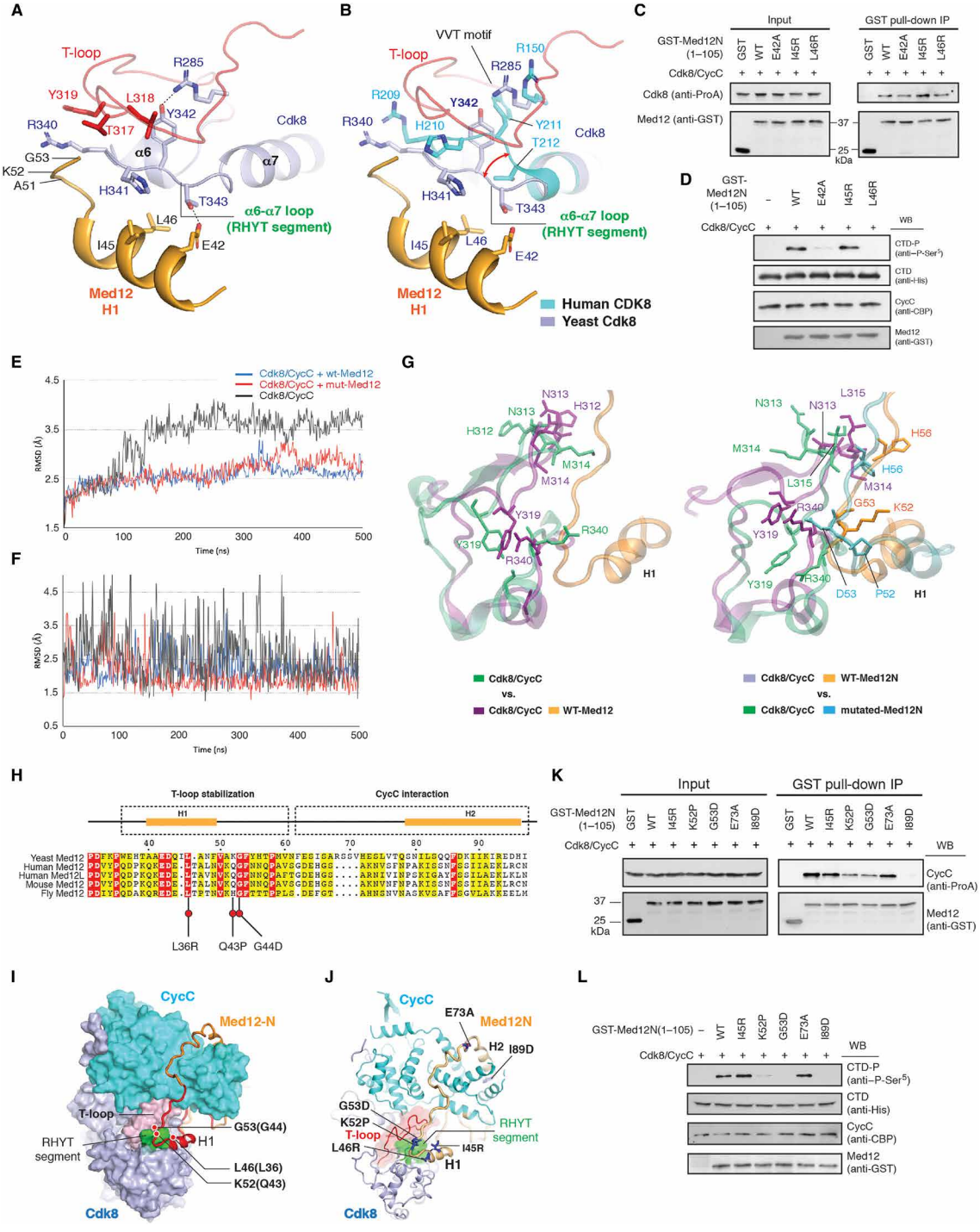

Fig. 4. Structural rearrangements of the RHYT segment and T-loop stabilization. (**A**) H1 of Med12 bound to yeast Cdk8. (**B**) Superimposition of yeast and human Cdk8 [Protein Data Bank (PDB ID): 3RGF] structures showing conformational differences of the RHYT segments. (**C**) Pull-down analysis for interactions between Cdk8/CycC and GST-Med12-(1–105). (**D**) Effects of WT or mutant GST-Med12-(1–105) on kinase activity of Cdk8/CycC. (**E** and **F**) RMSD plots of the T-loop and RHYT segment regions during molecular dynamics simulations. (**G**) Left: Superimposition of simulated models showing effects of Med12N binding on the T-loop and the RHYT segment regions of Cdk8. Cdk8 models simulated in the absence or presence of Med12N are colored in green or purple, respectively. Right: Superimposition of simulated models showing effects of mutant Med12N on the T-loop and the RHYT segment regions of Cdk8. (**H**) Sequence alignment of the N-terminal region of Med12. The identical and similar residues are highlighted by red and yellow, respectively. Three UL hotspot mutations of human MED12 (L36, Q43, and G44) are indicated by red dots. (**I**) Zoomed-in view of UL-linked MED12 driver mutations near Cdk8/CycC. The portion (residues 27 to 51) of human MED12 carrying recurrent UL-causing mutations is highlighted in red. The T-loop and RHYT segment of Cdk8 are shown in pink and green surfaces, respectively. Three human UL hotspot mutations are indicated by red dots. (**J**) Structure of Cdk8/CycC/Med12N. The mutations on Med12 are as indicated. (**K**) Pull-down analysis for interactions between WT and mutants of GST-Med12-(1–105). (**L**) Effects of WT and mutant derivatives of GST-Med12-(1–105) on kinase activity of Cdk8/CycC analyzed by Western blot.

points to the VVT motif. In addition, residue H210 (H341 in yeast Cdk8) is positioned such that it likely impinges on the T-loop. These factors might cause steric hindrance and T-loop destabilization. This could explain why all T-loops in the structures of human CDK8/CycC (determined in the absence of MED12/MED13) are mostly disordered (fig. S5D). To determine whether Med12 H1 is important for kinase activation, we engineered mutations in RHYT-interacting (E42A and L46R) or RHYT-noninteracting (I45R) residues (Fig. 4A) and assessed their impact on the ability of MED12N to bind and activate Cdk8/CycC. Compared to WT Med12N, mutant derivatives E42A and L46R exhibited no apparent differences in Cdk8/CycC binding activity (Fig. 4C) but markedly reduced Cdk8/CycC kinase activity (Fig. 4D). As expected, mutant derivative I45R exhibited no reduction, compared to WT Med12N, in Cdk8/CycC binding and kinase stimulatory activities (Fig. 4, C and D), as our structure revealed that I45 is not involved in RHYT binding. On the basis of these collective observations, we hypothesize that Med12 binding can elicit structural rearrangement of the Cdk8 RHYT segment, which, in turn, triggers stabilization of the T-loop into an active conformation.

To further investigate whether Med12N contributes to stabilization of the Cdk8 T-loop, we performed molecular dynamics simulations to assess flexibilities of the T-loop (residues 304 to 327) and RHYT segment (residues 339 to 344) using models for Cdk8/CycC or Cdk8/CycC/Med12N (residues 1 to 105) obtained from our CKM structure. We calculated the root mean square deviation (RMSD) values for small regions of interest to measure protein conformational stability over the course of their trajectories. Compared with Cdk8 bound by Med12N, we found that the T-loop of Cdk8/CycC alone exhibits higher averaged RMSD, indicating more flexibility in this region when Med12 is absent (Fig. 4E). Similarly, the RMSD of the RHYT region from Cdk8/CycC alone also becomes slightly higher overall and fluctuates more, reflecting the more transient nature of RHYT region to T-loop contacts when Med12N is not present to stabilize the RHYT segment (Fig. 4F). Notably, on the basis of the analysis of the root mean square fluctuation (RMSF) per residue, amino acids A339, R340, and H341 of the RHYT region, as well as Y319 of the T-loop, in Cdk8/CycC show higher RMSF, indicating greater flexibility during the molecular dynamics simulation when Med12N is not bound (fig. S6, A and B). In the absence of Med12N, the close interaction of Cdk8 residues Y319 (T-loop) and R340 (RHYT segment) is lost, and a region (residues 310 to 314) in the T-loop around F311, which is buried by a hydrophobic core formed in the presence of Med12, shows large structural changes (Fig. 4G, left, and fig. S6A). On the basis of these results, we believe that Med12, including H1 and its following residues (residues 51 to 53), contributes to the stabilization of the Cdk8 T-loop through contacts with the RHYT region, thereby enabling kinase function in the absence of canonical phosphorylation.

UL-linked mutations in Med12 alter residues that stabilize the Cdk8 T-loop

UL-linked alterations in human MED12, including missense mutations and in-frame deletions/insertions, cluster exclusively within the N-terminal portion of Med12, suggesting a deleterious impact on Cdk8/CycC kinase activity (Fig. 4H). Prior biochemical studies have shown that these mutations disrupt the ability of human MED12 to activate CDK8/CycC (*19*, *20*, *42*). Nonetheless, the molecular basis for these biochemical observations has remained obscure. In this regard, we recently postulated that UL-linked mutations in MED12 disrupt its ability to activate CDK8 by disrupting its direct association with CycC, leading to loss of allosteric activation. Notably, however, our structural analysis reveals instead that UL-linked mutations in human MED12, including hotspot mutations G44D, Q43P, and L36R (corresponding to yeast Med12 residues G53, K52, and L46, respectively), as well as in-frame insertions/deletions (variously spanning human residues 26 to 55; corresponding to yeast residues 37 to 64), map to a region next to the T-loop and RHYT segment of Cdk8 (Fig. 4I). For example, yeast Med12 G53 (corresponding to human MED12 G44, the most frequently mutated residue in UL) is positioned next to the interface between the T-loop and RHYT segment (Fig. 4I). Accordingly, pathogenic mutations at G44, Q43, and L36 of human MED12 are likely to alter interactions between MED12 and the CDK8 T-loop/RHYT segment required for T-loop stability and kinase activity.

To examine this possibility, we first assessed the impact of orthologous pathogenic mutations in Med12N on its ability to bind and activate Cdk8/CycC. To this end, we introduced into Med12N substitution mutations L46R, K52P, and G53D (corresponding to UL hotspot mutations L36R, Q43P, and G44D in human MED12; Fig. 4J) and thereafter examined these mutant derivatives for their respective abilities to bind and stimulate Cdk8/CycC activity using an in vitro pull-down assay. We also assessed three additional M12N mutant derivatives, including E73A and I45R, which are not involved in Cdk8/CycC binding, and I89D, which is involved in CycC binding (Fig. 4J). Compared to WT Med12N, mutant derivatives L46R, K52P, and G53D exhibited no apparent difference in Cdk8/CycC binding activity (Fig. 4, C and K) but markedly reduced Cdk8/CycC kinase activity (Fig. 4, D and L). This is consistent with our prior findings that MED12 binding is necessary but not sufficient for CDK8/CycC activation and suggests that mutations L46R, K52P, and G53D in Med12 affect T-loop stability, resulting in decreased Cdk8 kinase activity. As expected, mutant derivatives I45R and E73A exhibited no reduction, compared to WT Med12N, in Cdk8/CycC binding and kinase-stimulatory activities, as our structure revealed that they are not involved in Cdk8/CycC binding. Notably, mutant derivative I89D compromised both the Cdk8/CycC binding and kinase stimulatory activities of Med12N (Fig. 4, K and L), indicating that the Med12-CycC interface is critical to anchor MED12N and thus facilitate Cdk8 activation through direct Med12N-Cdk8 interactions.

To better understand how pathogenic mutations in Med12 disrupt Cdk8 kinase activity, we introduced mutations K52P and G53D (corresponding to human UL-linked mutations Q43P and G44D) into the Cdk8/CycC/Med12N model structure and performed molecular dynamics simulations to assess flexibilities within the Cdk8 T-loop and RHYT regions as a function of these Med12N mutations. We also included an additional Med12N mutation at residue E42 (E42A) since the corresponding residue (E33) in human MED12 is a hotspot for mutation in chronic lymphocytic leukemia (*43*). The RMSD data revealed similar stabilities for the T-loop and RHYT regions in both WT and mutant Cdk8/CycC/Med12N (Fig. 4, E and F). Notably, however, examination of the models showed that that the conformation of the RHYT region is altered in the mutant models (Fig. 4G, right). Furthermore, Cdk8 T-loop residues 313 to 315 and Y319 adopt altered conformations in the mutant compared to the WT models (Fig. 4G, right). Accordingly, we speculate that pathogenic mutations in Med12N stabilize the T-loop in a distinct conformation that is unfavorable for substrate phosphorylation, which could also explain why these mutations do not affect the binding of Med12N to Cdk8/CycC.

Med13 has an Ago architecture with unique structural features

In eukaryotes, Ago proteins (~100 kDa) play a central role in gene-silencing processes guided by small RNAs (*44*). The structures of Ago proteins reveal a common architecture composed of four globular domains (N, PAZ, MID, and PIWI) and two linker domains (L1 and L2), which form two lobes (N-PAZ and MID-PIWI) with a central nucleic acid–binding cleft between them (*45*). The PIWI domain adopts a typical RNase H fold with a set of catalytic residues in the active site, while the MID and PAZ domains are involved in 5′ and 3′ guide RNA binding, respectively (*45*). On the basis of our structural findings, described below, we categorize Med13 as a new Ago subfamily.

Med13 is located at the middle of the CKM and interacts with Med12 and CycC (Fig. 1F). Although Med13 is widely present among eukaryotes, its physiological role nonetheless remains poorly understood because of limited structural and functional information. On the basis of sequence analysis, the N- and C-terminal regions in Med13 are inferred to be connected by a large intrinsically disordered region (IDR). Furthermore, the C-terminal region of Med13 was previously predicted to have Ago MID and PIWI domains, thus classifying Med13 as a member of the PIWI protein family (*27*). Unexpectedly, our structure herein reveals that Med13, in addition to MID and PIWI domains, is composed of several additional domains that define classical Argonaute (Ago) proteins (Fig. 5A and movie S3) (*28*, *45*). Thus, despite low overall sequence homology between Med13 and Ago proteins, the structure of Med13 nonetheless revealed that four globular domains (N, PAZ, MID, and PIWI) and two linker domains (L1 and L2) form two lobes with a narrow central channel (Fig. 5B). The large IDR (residues 313 to 814) inferred from sequence analysis, and absent in typical Ago proteins, lies between the PAZ and L2 domains and is indeed disordered in the density map. Although Med13 adopts the bilobal architecture characteristic of ago proteins, no density corresponding to DNA or RNA was found within its central channel. This contrasts with previously reported eukaryotic Ago structures wherein the 5′ and 3′ guide RNA–binding sites and the central channel are typically occupied by cell-derived small RNAs following protein purification (*46*–*52*), suggesting that the current Med13 structure within the CKM represents a nucleic acid–free (apo) conformation.

Notably, while Med13 has an overall Ago architecture, our structural analysis nonetheless reveals several unique structural features that are not observed in typical Ago proteins. We identified four unique insertions (ins)—two within the PAZ domain (PAZ-ins1 and PAZ-ins2), one between the MID and PIWI domains (MID-PIWI-ins), and one within the PIWI domain (PIWI-ins) (Fig. 5, A and B, and fig. S7A). Among these four insertion segments, three (PAZ-ins2, MID-PIWI-ins, and PIWI-ins) are involved in interactions with Med12 and contribute to stabilizing the CKM (fig. S7B), whereas the fourth (PAZ-ins1) is positioned into and thereby narrows the central cleft (fig. S7C). By comparing both the Med13 and human Ago 2 (hAgo2) structures, we found that all of their individual domains can be superimposed very well (fig. S7, D and E). However, their respective PAZ and PIWI domains, as well as their L2 domains, show greater divergence due to Med13-specific insertions and conformational differences. In Med13, the N-terminal region of the L2 domain (L2-N) adopts a hairpin structure, containing two α helices (α7 and α8), which extends from the rest of the domain, whereas the corresponding region in hAgo2 forms two α helices in an L-shaped conformation adjacent to the elongated C-terminal region of L2 (fig. S7E).

The L2 domain occupies the central channel of Med13

In hAgo2, guide RNAs are threaded through the central channel, and their 5′ and 3′ ends are recognized by the MID and PAZ domains, respectively (*47*, *48*). However, in contrast to hAgo2 structures, the corresponding nucleic acid–binding regions in our Med13 structure show distinctive features. The L2-N in Med13, which is a Med13-specific hairpin, starts by forming a short α helix (α7) in the PAZ domain, runs toward the MID domain across the central channel, and then inserts an α helix (α8) into the interface between the MID and PIWI domains (Fig. 5C). In hAgo2, the L2 domain instead adopts the typical conformation found in Ago proteins that does not run across the central cleft (Fig. 5D). Furthermore, in Med13, the central channel through which guide RNA would be threaded in hAgo2 is instead bound by a linker region between the α7 and α8 of L2-N (Fig. 5C). Last, in Med13, helix α7 and a coil fragment adjacent to helix α8 of L2N occupy the corresponding regions in hAgo2 that are bound by the 3′ and 5′ ends of the guide strand RNA, respectively (Fig. 5, E and F). These observations led us to propose that Med13 L2-N mimics Ago-bound guide RNA. Together, these structural considerations indicate that Med13 is inaccessible to nucleic acids because the central channel is occupied by L2-N. The implications of these unique structural features will be discussed subsequently.

DISCUSSION

In this study, we provide a near-atomic resolution structure of the entire CKM, one that redefines prior subunit organization, explains how Cdk8/CycC is recognized and activated by Med12, and newly identifies Med13 as a novel member of the Ago protein family. The fact that Cdk8 lacks a canonical phosphorylation residue in its T-loop and also forms a large complex with CycC, Med12, and Med13 distinguishes its mechanism of activation from other CDK family proteins. Our structural and biochemical studies reveal that Med12 forms critical contacts with both Cdk8 and CycC and establish a novel molecular mechanism for how Med12 activates Cdk8 kinase. The observation that UL-linked MED12 mutations localize to the vicinity of the Cdk8 T-loop and RHYT segment suggests that disruption of Mediator kinase activity is a major biochemical defect arising from these pathogenic mutations, providing new molecular insight into disease etiology. Accordingly, our structure also provides further rationale for targeting the MED12-CDK8/CycC interface for treatment of diseases caused by dysregulation of Cdk8 kinase activity.

Our structure shows that CycC, including its the conserved groove, provides a large surface area for extensive interactions with Med12. Biochemical analyses confirmed these interactions to be critical for the ability of Med12 to bind and activate Cdk8/CycC. Thus, targeted mutations in residues identified by structural analysis to comprise the CycC-Med12 interface were found to disrupt Med12 binding and Cdk8 activation. In addition, while clearly necessary, Med12 binding is not sufficient for Cdk8/CycC activation since we also show that mutations of Med12 residues (H1 and flanking residues) that are not involved in CycC interaction, including oncogenic Med12 mutations L46R, K52P, and G53D, disrupt the ability of Med12 to activate, but not to bind, Cdk8/CycC. These findings are consistent with our prior biochemical observations using human CKM proteins (*19*, *20*) and indicate an additional step beyond CycC binding that is required for Med12-dependent Cdk8 activation—one

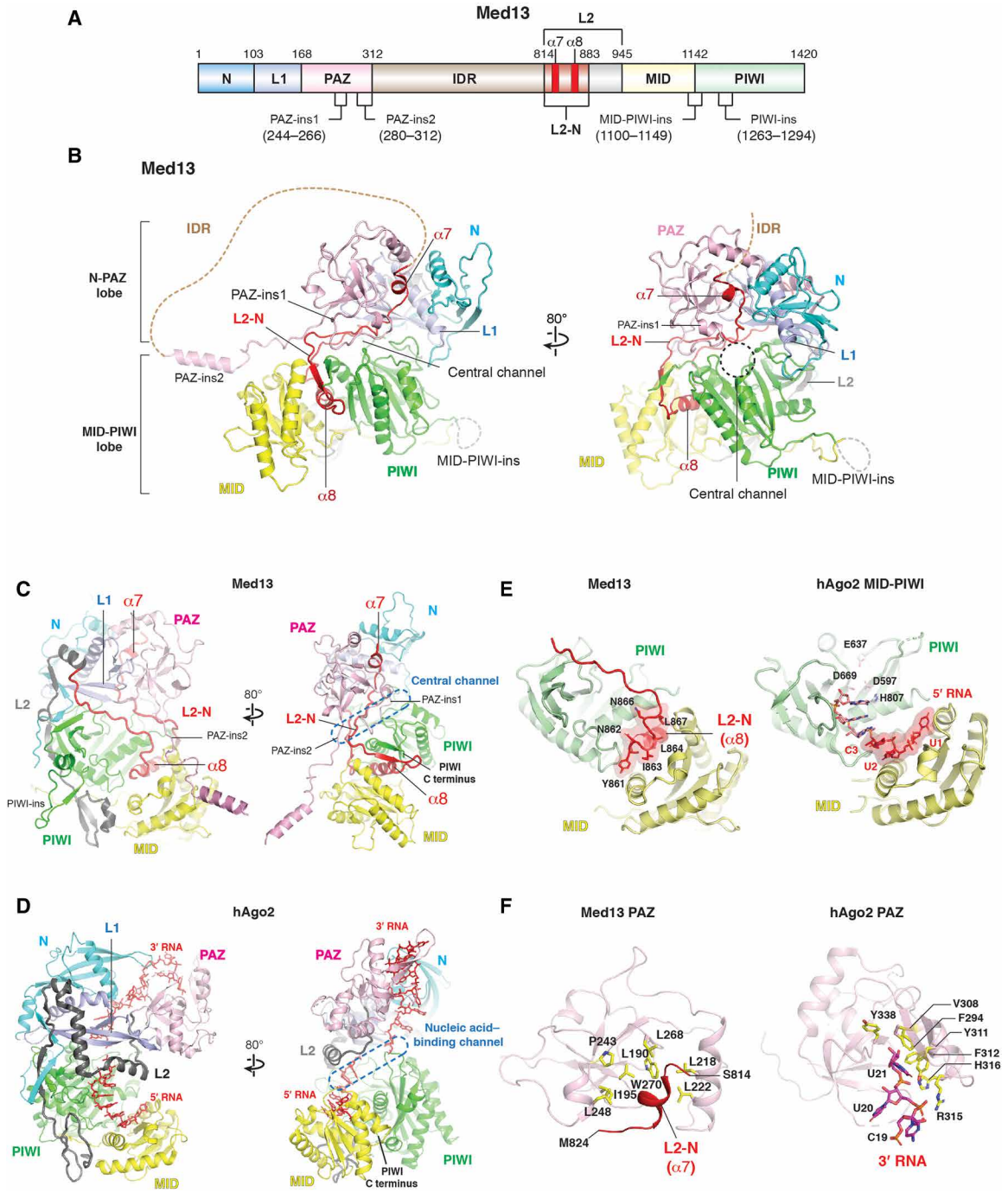

Fig. 5. Structure of Med13 Ago. (**A**) Domain organization of Med13. (**B**) Structure of Med13. Colors are as in (A). The missing IDR is indicated by dashed lines. (**C**) Two views of Med13 structure. The L2-N of Med13 is colored in red. The central channel is indicated by a dashed oval. (**D**) Two views of hAgo2 structure (PDB ID: 4W5N). The 5′ and 3′ guide RNAs are indicated (red sticks). The L2 domain is colored in dark gray. (**E**) Left: A portion of Med13 L2-C (red) occupies the 5′ nucleic acid–binding site at the MID domain. The residues in Med13 overlapped with the guide RNA in hAgo2 are shown in surface. Right: 5′ guide RNA (red sticks) bound at the MID and PIWI domain of hAgo2. The first three 5′ RNA nucleotides (U1, U2, and C3) are labeled. The catalytic tetrad residues in the PIWI domain are indicated. (**F**) Left: Residues in PAZ of Med13 involved in contacts with the N-terminal portion of L2-N (red) in Med13 are indicated. Right: Residues in PAZ of hAgo2 involved in interaction with 3′ guide RNA are indicated.

dependent on Med12 residues frequently mutated in UL and other tumors. Here, we identify this additional activation step to be the Med12-dependent stabilization of the Cdk8 T-loop with important implications for Cdk8-driven disease. In this regard, our studies revealed that the interaction of Med12H1 and its flanking residues (51 to 53) with the Cdk8 RHYT segment directs the latter to engage in a precise network of intramolecular interactions with the Cdk8 T-loop, leading to its stabilization in an activated conformation

(Fig. 6A). Thus, we observed the Cdk8 T-loop to be flexible in the absence of Med12 (fig. S5D) and unfavorably poised for substrate binding and phosphorylation. By contrast, in the presence of Med12, the Cdk8 T-loop was found to be structured in an activated conformation with space sufficient to accommodate target substrates (Fig. 6A). Notably, the fully activated conformation of Cdk8 is realized only upon stabilization of its T-loop through extensive interactions occurring between the Cdk8 RHYT segment and Med12. Thus, binding of Med12 H1 and its flanking residues (amino acids 51 to 53) to the RHYT segment triggers a structural rearrangement in the latter; in turn, the rearranged RHYT segment, together with the Med12 residues 54 to 56 following H1, contributes to stabilization of the Cdk8 T-loop, thereby enabling kinase activity in the absence of canonical T-loop phosphorylation. Although our findings establish a novel mechanism for Cdk8 activation requiring Med12, they also raise an important question regarding whether and how the kinase activity of Med12-bound Cdk8/CycC is regulated. In this regard, it is notable that human MED12 has been shown to associate with certain activating noncoding RNAs that are able to stimulate the kinase activity of CDK8 toward histone H3 Ser^{10} (*22*, *25*). Although detailed mechanisms remain to be clarified, it is possible that interactions of MED12 with other factors may affect the kinase activity and substrate specificity of CDK8.

Our yeast CKM structure is not generally consistent with a recently reported study on the human CDK8/CycC/MED12N complex analyzed by XL-MS experiments, which concluded that MED12 makes extensive contacts with both the N- and C-lobes of CDK8 without substantially interacting with CycC (*53*). In our CKM structure, however, Med12N interacts extensively with CycC and contacts Cdk8 only at its C-lobe (Fig. 3A). We speculate that this discrepancy could be attributed to Med13, which was present in our CKM structure but absent in the prior XL-MS–based study. In our yeast CKM structure, the Med13 MID-PIWI-ins makes several contacts with the interface between Med12 H2 and CycC (Fig. 3A and fig. S4H), suggesting that Med13 could stabilize the Med12-CycC interaction. In the absence of MED13, it is likely that MED12N may not be able to stably wrap around CDK8/CycC, leading to conformational flexibility that precluded detectable contacts between MED12 and CycC in prior XL-MS experiments. Our findings are supported by near-atomic level structural determination and XL-MS–based confirmation carried out with the intact CKM. Considering significant protein sequence conservation between human and yeast Cdk8, CycC, and Med12 (N-terminal region), we believe that the interaction mode between Med12 and Cdk8/CycC is likely conserved among species.

Our studies further clarify the molecular basis of MED12 in human disease. In this regard, numerous pathogenic alterations, including germline mutations causing the intellectual disability disorders FG, Lujan, and Ohdo syndromes, as well as somatic driver mutations leading to UL, breast fibroadenomas, and prostate cancer, have been found in human MED12 (*31*–*35*, *42*, *54*, *55*). In general, different types of disease mutations are mapped on different regions of Med12, indicating that disease type–specific mutations in MED12 may differentially affect its function (fig. S8A). To clarify molecular mechanisms underlying disease type–specific mutations in MED12, we mapped pathogenic MED12 mutations onto our yeast CKM structure based on sequence alignment (fig. S8B). Although we did not assign residues for the Med12 HEAT domains (2 to 5) within the CKM, we found that MED12 mutations linked to FG, Lujan, and Ohdo syndromes, as well as prostate cancer, are nonetheless localized in the H-lobe (fig. S8B). This suggests that these mutations may influence interactions of MED12 with other factors but not CDK8/CycC.

By contrast, UL-linked alterations in MED12 were mapped exclusively within Med12 H1 and its flanking residues that critically interface with the Cdk8 RHYT/T-loop region, suggesting a deleterious impact on MED12-dependent CycC/Cdk8 activation (fig. S8B). Here, we confirm this prediction and, thus, clarify the mechanistic basis by which pathogenic mutations in MED12 drive tumorigenesis through CKM dysfunction. Curiously, our molecular dynamics simulations indicate that driver mutations in Med12, as opposed to triggering T-loop destabilization, instead promote reconfiguration of the Cdk8 T-loop into a stable conformation incompatible with efficient substrate binding and/or phosphorylation. This could effectively disable Cdk8 kinase activity, and, thus, circumvent a critical barrier to cellular transformation, while also preserving its structural integrity and retention of a critical kinase-independent (scaffolding) function required for cell viability (*56*, *57*). Ongoing studies designed to elucidate the structure and function of CKM variants incorporating oncogenic Med12 mutant derivatives should clarify these and other pressing issues.

We found that Med13 has an Ago-like bilobal architecture, which implies an additional capability for CKM interaction with nucleic acid duplexes. Since nucleic acids were not observed in the central channel, the conformation of the current Med13 structure is more similar to the closed form of prokaryotic apo-Ago proteins (*29*, *58*–*60*). The PIWI domains of Ago proteins adopt an RNase H fold (*28*), but their slicing capability depends on the existence of the catalytic DEDD or DEDH tetrad in the active site (*46*). For instance, eukaryotic slicer Ago proteins, such as *Kluyveromyces polysporus* Ago, hAgo2, and hAgo3, have the catalytic tetrad in the active site (fig. S7F, top) (*46*, *51*). Our structure described herein shows that the Med13 PIWI domain retains none of the previously identified catalytic residues (fig. S7F, bottom), suggesting that Med13 lacks endonucleolytic activity. However, similar to other human and yeast Ago proteins, Med13 does carry some positively charged residues along the central channel on the surface of the PIWI and MID domains (fig. S7G). These structural observations suggest that the channel of Med13 retains nucleic acid–binding ability but is nonetheless occupied by L2-N (Fig. 5, C, E, and F). This contradiction could be explained if the current structure reflects an autoinhibition state, one in which the central channel cannot interact with nucleic acids that absent a regulated release of the coil fragments of L2-N. Rearrangement of L2-N may enable the central channel of Med13 to capture nucleic acid duplexes without cleavage, given that the Med13 PIWI domain lacks a catalytic tetrad. Supporting this, the CKM was found to preferentially associate with highly transcribed genes in yeast (*61*, *62*) that have the propensity to generate DNA–small RNA hybrids. In this regard, it is perhaps notable that deletion of Med13 in yeast has been implicated in R-loop formation and genomic instability (*63*). On the basis of these observations, the CKM might be involved in the modulation of high-level gene expression through Med13. On the other hand, Med13 might bind to an RNA stem region in long noncoding RNAs. This ability could correlate with the observation that the CKM is located in enhancer elements genome wide (*64*) and might also be involved in enhancer-promoter looping through interactions with enhancer RNAs (*22*). Further studies will be required to investigate whether and what type of nucleic acid duplex binds to Med13 and how such a role regulates the transcription process.

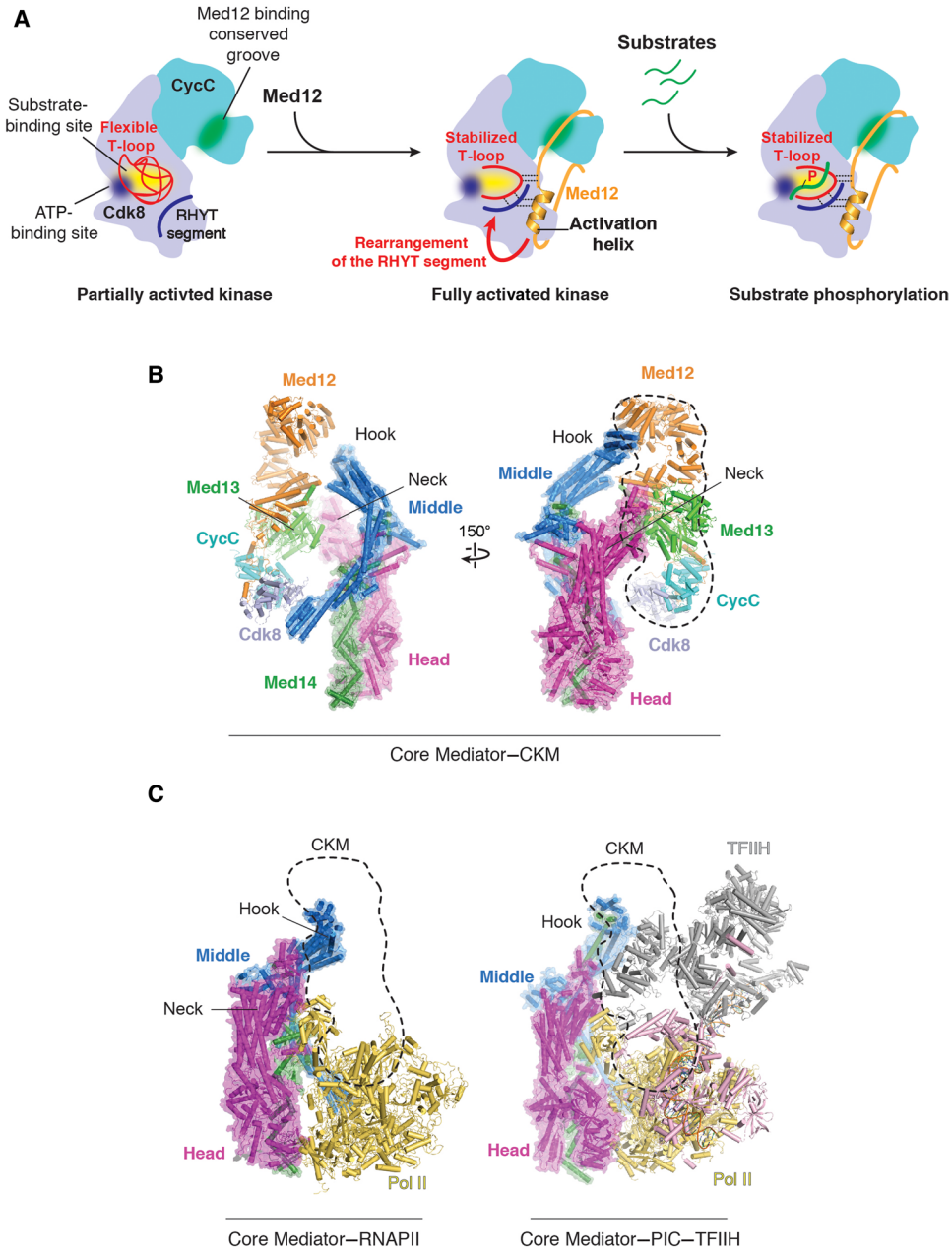

Fig. 6. Models for Med12-dependent Cdk8 activation and Core Mediator–CKM complex. (**A**) Model for Cdk8 kinase activated by Med12N. Left: In the absence of Med12, CycC-bound Cdk8 is in a partially activated conformation. The T-loop (red) is disordered, thus hindering substrates from entering into the catalytic site (yellow). A highly conserved region in CycC is highlighted in green. Middle: Binding of Med12 to the conserved groove in CycC allows its H1 to trigger rearrangements of the RHYT segment, leading to stabilization of the Cdk8 T-loop. Right: Stabilized T-loop leads to formation of platform for substrate phosphorylation. (**B**) Model of the Core Mediator–CKM complex. The subunits of Core Mediator are highlighted by surface representations. The CKM is highlighted by a dashed outline. (**C**) Location of the CKM (dashed outline) on Core Mediator overlaps with RNAPII and TFIIH. Left: Structure of the Core Mediator–RNAPII complex (PDB ID: 5U0S). Right: Structure of the Core Mediator–PIC–TFIIH complex (PDB ID 5OQM). RNAPII and TFIIH are colored in yellow and gray, respectively. The remaining subunits of the PIC are colored in pink.

Prior studies have reported that the CKM is able to suppress activated transcription in vitro and precludes interaction of RNAPII with the Mediator (*5*, *9*, *21*). To understand how the CKM forms a complex with Core Mediator, we developed a model by fitting our CKM and previously reported Core Mediator structures into a negative-stain EM map of yeast Mediator-CKM complex (fig. S9) (*3*, *5*). This model indicates that the CKM is localized to the top portion of Core Mediator at which Med12 and Med13 subunits are close to the Hook and Neck regions (Fig. 6B). This is in agreement with previous biochemical observations that human MED12 and MED13 are able to associate with a part of Mediator Middle module subunits (*5*). Notably, when compared with cryo-EM structures of RNAPII–Core Mediator and TFIIH–PIC–Core Mediator (Fig. 6C) (*3*, *65*), our model reveals that the location of CKM on Core Mediator partially

overlaps with those of both RNAPII and TFIIH, suggesting steric hindrance as the basis by which the CKM precludes interactions of Pol II and TFIIH with the Mediator and suppresses the activated transcription. A high-resolution structure of the Mediator-CKM complex will reveal more detailed information about how the CKM interacts with Mediator and represses transcription.

The CKM constitutes a large sophisticated and multifunctional macromolecular complex. Here, we have shown that in addition to a noncanonically activated and oncogenic mutation-sensitive cyclin-dependent kinase, the CKM comprises both an Ago-like Med13 and an elongated Med12 subunit with a HEAT core that offers great potential for regulatory interactions. The capabilities of the CKM to phosphorylate transcription factors, to associate with activating noncoding RNAs, and to regulate Mediator-RNAPII interaction demonstrate the broad influence of CKM on RNAPII gene transcription. Further studies are warranted to determine how the structural and functional complexity of the CKM are exploited to expand the regulatory potential of Mediator in transcriptional regulation.

MATERIALS AND METHODS

S. cerevisiae strains

All yeast strains used in this study were constructed from a protease-deficient yeast strain BJ2168 (American Type Culture Collection, 208277). Yeast gene manipulations, including TAP, hemagglutinin (HA), and Flag tagging, subunit deletion, and truncation, were carried out by using a standard polymerase chain reaction (PCR)–based transformation protocol (*66*). To generate a TAP-tagged strain of CycC, the pBS1479 plasmid was used to introduce a TAP tag at the C terminus of the targeted protein. The pFA6a-Flag-kanMX6 and pHyg-AID-HA plasmids were used to introduce a 5xFLAG tag and 1× HA tag at the C terminus of Med12 and Med13, respectively. For subunit deletion or truncation, a PCR-amplified KanMX6 or Hyg cassette was used to replace either the entirety of an open reading frame or a specific region. The tagged yeast strains were confirmed by Western blot analysis. The strains with subunit deletion or truncation were verified by DNA sequencing. Yeast strains used in this study are listed in table S1.

Cloning, expression, and purification of recombinant Med12 proteins

DNA fragments encoding residues 1 to 105, 106 to 419, 420 to 596, 597 to 789, 789 to 1335, and 1336 to 1427 of yeast Med12 were generated by PCR amplification using full-length Med12 DNA as a template and ligated into pGEX6P-1. The I45R, K52P, G53D, E73A, and I89D mutants were generated using the pGEX6P-1-Med12-(1–105) WT plasmid as a template. All constructs were verified by DNA sequencing. WT and mutants of Med12-(1–105), fused to the C terminus of glutathione *S*-transferase (GST) protein, were expressed in *Escherichia coli* BL21(DE3) by addition of IPTG (isopropyl-β-D-thiogalactopyranoside) at a final concentration of 1 mM for 3 hours at 37°C. After induction, *E. coli* cells were harvested and lysed by sonication in buffer A [1× phosphate-buffered saline (PBS) (pH 7.4), 2 mM β-mercaptoethanol, 10% glycerol, and 0.1% NP-40] containing protease inhibitors (Roche). The lysate was clarified by high-speed centrifugation at 20,000 rpm for 30 min using a Beckman 45 Ti rotor, and the resulting supernatant was incubated with glutathione Sepharose 4B beads (GE Healthcare) for 30 min at 4°C. Beads were washed three times using buffer A. Proteins were eluted by buffer A containing 10 mM glutathione and analyzed by SDS-PAGE. Purified proteins were subjected to the following kinase assay experiments. For GST pull-down assays, each of the Med12 fragments or mutants, fused to the C terminus of GST protein, was expressed in *E. coli* BL21(DE3) followed by the procedure as described below.

GST pull-down assay

Yeast cells of CycC-TAP/Med12Δ/Med13Δ from 20 liters of 2× YPD (yeast extract, peptone, and dextrose) medium were used to obtain cell extract that contains endogenous Cdk8/CycC proteins. To examine the interaction between Cdk8/CycC and Med12 fragments, lysates of *E. coli* cells from 50 ml of LB medium expressing GST alone, GST-Med12-(1–105), GST-Med12-(106–419), GST-Med12-(420–596), GST-Med12-(597–789), GST-Med12-(789–1335), or GST-Med12-(1336–1427) were clarified by high-speed centrifugation. Each supernatant was incubated with 20 μl of glutathione Sepharose 4B beads (GE Healthcare) in buffer A containing protease inhibitors for 30 min at 4°C. The bead resin was washed three times with buffer A followed by the addition of 1 ml of yeast cell extract (0.5 mg/ml; CycC-TAP/Med12Δ/Med13Δ) and then incubated for 30 min at 4°C. The resin was washed five times using buffer A and then eluted using 50 μl of elution buffer A containing 10 mM glutathione. The eluates were analyzed by SDS-PAGE and Western blotting using anti-GST antibodies (GenScript, A0086640) and anti–protein A antibodies (Sigma-Aldrich, P1291). The same procedure was performed as described above to analyze the interaction between Cdk8/CycC and wild type or mutants (E42A, I45R, L46R, K52P, G53D, E73A, or I89D) of GST-Med12-(1–105).

FLAG immunoprecipitation assays

pFastBac Dual plasmids carrying WT or mutant (S210E, A227R, or F235E in CycC or D410R or I449E in Cdk8) yeast Cdk8-FLAG/CycC-6xHis were transformed into DH10Bac competent cells (Invitrogen). The isolated recombinant bacmid DNAs from white colonies were used for transfection of Sf9 insect cells. After three rounds of viral amplification, high-titer baculoviruses (P3) were used for infection of High Five cells (Invitrogen). After 48 hours after infection, 50 ml of cells was harvested and lysed with binding buffer B [20 mM Hepes (pH 7.5), 300 mM NaCl, 0.1% NP-40, 0.1 mM EDTA, 2 mM β-mercaptoethanol, 10% glycerol, and cOmplete protease inhibitors (Roche)] using a dounce homogenizer at 4°C. Lysates were clarified by high-speed centrifugation at 20,000 rpm for 30 min. Supernatants containing WT or mutant yeast Cdk8-FLAG/CycC-6xHis were subjected to FLAG immunoprecipitation (IP) for 1 hour at 4°C in buffer B. The FLAG bead resin was washed three times with buffer B followed by the addition of 1 ml of *E. coli* cell extract [0.5 mg/ml; GST or GST-Med12-(1–105)] and then incubated for 1 hour at 4°C. The resin was washed five times using buffer B and then eluted using 50 μl of elution buffer B containing 1× FLAG peptide (200 μg/ml). The eluates were analyzed by SDS-PAGE and Western blotting using anti-GST antibodies (GenScript, A0086640), anti–FLAG M2 antibodies (Sigma-Aldrich, F1804), and anti-His antibodies (R&D Systems, MAB050).

Kinase assay

The CTD of yeast RNAPII (residues 1535 to 1733) with a C-terminal 6× His-tag was fused to the C terminus of GST. GST-CTD-His6 was expressed in *E. coli* and purified using glutathione Sepharose 4B beads (GE Healthcare) following standard procedures. CKM and

Cdk8/CycC proteins were purified from CycC-TAP and CycC-TAP/Med12Δ/Med13Δ yeast cells, respectively, by ammonium sulfate precipitation and TAP purification procedures, as described (*7*). Purified Cdk8/CycC was confirmed by MS showing absence of Med12 and Med13 (data S2). Purified CKM (100 ng) or Cdk8/CycC (25 ng) was incubated at 30°C for 30 min in kinase buffer (100 μl) containing 1× PBS (pH 7.4), 10 mM $MgCl_2$, 1 mM ATP, and purified GST-CTD-His6 substrate. Reactions were terminated by addition of SDS sample buffer. The samples were processed by SDS-PAGE and analyzed by Western blotting using anti-His antibodies (R&D Systems, MAB050), anti-GST antibodies (GenScript, A0086640), and anti-CBP (Calmodulin Binding Protein) antibodies (Sigma-Aldrich, 07482). The antibody that recognizes phosphorylated Ser^5 of CTD (GenScript, A10634) was used to detect CTD phosphorylation. To assay effects of Med12N on kinase activity of Cdk8/CycC, reactions were carried with 60 ng of purified Cdk8/CycC and 250 or 1 μg of purified GST-Med12-(1–105) at 30°C for 30 min in kinase buffer (100 μl) containing 1× PBS (pH 7.4), 10 mM $MgCl_2$, 1 mM ATP, and purified GST-CTD-His6 substrate. To assay effects of Med12 mutants on kinase activity of Cdk8/CycC, we incubated 60 ng of purified Cdk8/CycC with 600 ng of purified WT, I45R, K52P, G53D, E73A, or I89D GST-Med12-(1–105) in the same kinase reaction buffer (100 μl) for 30 min at 30°C. The reactions were terminated and analyzed by the same procedure as described above.

IP assay from yeast cells

Yeast cells of BJ2168, CycC-TAP/Med12-5FLAG/Med13-HA, and CycC-TAP/Med12(1345–1427)Δ-5FLAG/Med13-HA from 50 ml of cultures were harvested by centrifugation (4000*g*, 10 min, 4°C). Harvested cells were washed twice with Milli-Q H_2O, resuspended in 1 ml of binding buffer [20 mM Hepes (pH 7.6), 500 mM NaCl, 0.1% NP-40, 5 mM β-mercaptoethanol, 10% glycerol, 0.5 mM EDTA, and protease inhibitors], and lysed using BeadBeater for 5 min at 4°C. Cell lysates were then centrifuged at 38,000 rpm for 30 min using a Beckman SW60 Ti rotor. Supernatants were collected and subjected to IP using 20 μl of IgG-Sepharose resin (GE Healthcare) for 1 hour of binding at 4°C in the binding buffer. After binding, reactions were washed five times using 0.5 ml of binding buffer without protease inhibitors and followed by tobacco etch virus (TEV) protease cleavage for 1 hour at 20°C. The elutes were processed by SDS-PAGE and analyzed by Western blotting using anti-HA antibodies (Sigma-Aldrich, 11867423001), anti–Flag M2 antibodies (Sigma-Aldrich, F1804), and anti-CBP antibodies (Sigma-Aldrich, 07482).

Yeast CKM purification for structure determination

CycC-TAP–tagged yeast cells were grown in 50 liters of 2× YPD medium. Cells were harvested, washed, and frozen using liquid nitrogen followed by a blending process. Whole-cell extract was prepared starting from 800 g of broken-cell powder as described (*5*). Briefly, lysed cells were resuspended in purification buffer [100 mM tris-HCl (pH 7.8), 500 mM ammonium sulfate, 2 mM EDTA, 5 mM β-mercaptoethanol, 10% glycerol, and protease inhibitors] followed by ammonium sulfate precipitation. The pellet containing CKM was dissolved using immunoglobulin G (IgG) binding buffer [25 mM Hepes (pH 7.4), 200 mM NaCl, 0.5 mM EDTA, 2 mM β-mercaptoethanol, 10% glycerol, 0.01% NP-40, and protease inhibitors] followed by high-speed centrifugation at 42,000 rpm for 30 min using a Beckman 50.2 Ti rotor. The supernatant was incubated with 4 ml of IgG-Sepharose beads (GE Healthcare) for 4 hours at 4°C. After incubation, the column was washed with buffer [25 mM Hepes (pH 7.4), 200 mM NaCl, 0.5 mM EDTA, 2 mM β-mercaptoethanol, 10% glycerol, 0.01% NP-40, and 1 mM dithiothreitol (DTT)] followed by the addition of TEV protease incubated overnight at 4°C. The CKM was then eluted in buffer [25 mM Hepes (pH 7.4), 200 mM NaCl, 0.5 mM EDTA, 2 mM β-mercaptoethanol, 10% glycerol, and 0.01% NP-40] followed by ion exchange Q chromatography. The peak fractions were collected and concentrated (Vivaspin, 50 kDa, GE Healthcare) for preparation of cryo-EM specimens.

Cryo-EM data collection and image analysis

Briefly, 3.0 μl of WT CKM (~1 mg/ml) in buffer [25 mM Hepes (pH 7.4), 200 mM NaCl, and 0.005% NP-40] were directly applied to grow discharged 400-mesh C-flat holey carbon grids (EMS) with 2 μm by 1 μm holes. After incubation for 10 s, each grid was blotted for 3 to 4 s at 4°C with 100% humidity and vitrified in liquid ethane using a Vitrobot Mark IV (FEI). The grids were imaged on a 300-kV Titan Krios electron microscope (FEI) using a GIF Quantum K2 direct electron detector (Gatan) operating in counting mode. Images were automatically collected at 0.8- to 3.5-μm underfocus values with a nominal pixel size of 1.07 Å per pixel using EPU (FEI). Each image was exposed for 8 s with a total dose of approximately 65 electrons/$Å^2$, which was fractioned into 40 frames. MotionCor2 was used to align frames (*67*). The parameters of contrast transfer function (CTF) for each image were estimated using the program Gctf (*68*). Images with an estimated resolution better than 7 Å and underfocus values between 0.8 and 3.5 μm were selected, resulting in 15,075 micrographs (table S2). An initial particle picking was carried out using template-free picking on ~1000 micrographs followed by 2D clustering in RELION (*69*). Five of 2D class averages showing different views of CKM were used as templates to perform template-based picking on the 15,075 micrographs using Gautomatch (*70*), resulting in a total of 815,542 images. 2D clustering in cryoSPARC (*71*) was carried out to obtain a stack of 230,748 images that was used to generate initial 3D models of CKM. 3D classification was carried out in RELION (*69*) to identify a set of 138,178 images that was run through 3D refinement, Bayesian polishing, and CTF refinement to obtain a 3D map of CKM at 4.4-Å resolution. For Kinase- and Central-lobes of the CKM, the 138,178 images were further 3D classified and refined with a focused mask that covered both lobes, resulting in a final map of Kinase/Central-lobes at 3.8-Å resolution. For the H-lobe of CKM, we also started from the 138,178 images and performed 3D classification with a mask that only covered the H-lobe using cryoSPARC and RELION (*69*, *71*). A final stack of 36,691 images were selected to run 3D refinement with the same mask, resulting in a final H-lobe map at 4.9-Å resolution. The resolutions of final 3D maps were estimated using gold-standard Fourier shell correlation curves with 0.143 criteria (*72*). RELION was used to calculate local resolutions. An image analysis procedure for the cryo-EM data of CKM is shown in fig. S1.

CKM modeling and refinement

To build the CKM atomic model, we started by rigid-body fitting the x-ray structure of human CDK8/CycC [Protein Data Bank (PDB ID): 3RGF] (*38*) into the cryo-EM map of Kinase/Central-lobes using Chimera (*73*). The model building of yeast Cdk8/CycC was facilitated by sequence alignments of Cdk8/CycC between yeast and human.

The rest portion of the Kinase/Central-lobes map was of sufficient quality for ab initio model building for the N- and C-terminal regions, and HEAT-1 domain of Med12, and Med13, facilitated by secondary structure predictions from PHYRE2 web server (*74*). For model building of the H-lobe, the main-chain trajectory of Med12 HEAT domains (2 to 5) was able to be traced in the map. Alanine residues were assigned to this model. The model building and adjustments were done using Coot (*75*). Refinement of the Kinase/Central and H models against their corresponding cryo-EM maps were done by using the real-space refinement in Phenix (*76*). Both models built from two cryo-EM maps were combined to obtain an overall CKM model. In the final CKM model, amino acids for Cdk8 (1 to 47, 97 to 173, 190 to 194, 372 to 374, and 490 to 555), CycC (1, 46 to 56, 245 to 260, and 319 to 323), Med12 (1 to 3, 297 to 308, 1026 to 1068, and 1327 to 1343), and Med13 (1 to 4, 313 to 813, 1123 to 1141, and 1401 to 1420) were not built because of missing or poor densities. The connection that contains 17 missing residues (1327 to 1343) between Med12 HEAT-5 and Med12C is disordered with a distance of ~20 Å. The final overall model was validated using MolProbity (table S2) (*76*). All molecular graphic figures, including overall and local density maps, were made by Chimera or PyMOL.

XL-MS analysis of the CKM

The yeast CKM purified by ion exchange Q chromatography was dialyzed into a buffer containing 50 mM Hepes (pH 7.9), 200 mM NaCl, 2 mM β-mercaptoethanol, 0.01% NP-40, and 10% glycerol. The protein sample was resuspended with a disuccinimidyl dibutyric urea (DSBU) cross-linker (6 mM final, Thermo Fisher Scientific) and incubated for 90 min on ice. The reaction was quenched with ammonium bicarbonate and further incubated for 30 min on ice. Cross-linked proteins were reduced with 10 mM DTT for 30 min at 30°C, followed by alkylation with iodoacetamide (50 mM final, Sigma-Aldrich) for 30 min at 30°C. The proteins were processed by S-Trap (ProtiFi) with its recommended protocol: with trypsin in 1:10 (w/w) enzyme-to-protein ratio for an hour at 30°C. Eluted peptides were dried under vacuum and resuspended with the peptide fractionation elution buffer: LC-MS (liquid chromatography–MS)–grade 70% (v/v) water, 30% (v/v) acetonitrile (ACN), and 0.1% (v/v) trifluoroacetic acid (TFA). Peptide fraction was performed on ÄKTA pure 25 with Superdex 30 Increase 3.2/300 (GE Healthcare) at a flow rate of 30 μl min^{-1} of the elution buffer with a 100-μl fraction volume. Fractions containing enriched cross-linked peptides, which were empirically determined by the elution profile, were retained and dried under vacuum and resuspended with 0.1% (v/v) TFA containing LC-MS–grade water for MS analysis. Each fraction was analyzed on a Q Exactive HF mass spectrometer (Thermo Fisher Scientific) coupled with Dionex UltiMate 3000 UHPLC system (Thermo Fischer Scientific) with an in-house C18 column. Half of each sample amount was injected for the analysis and separated on a 90-min gradient: mobile phase A [99.9% water with 0.1% formic acid (Sigma-Aldrich)]; mobile phase B (80% ACN with 0.1% formic acid); starting 5% B, increased to 45% B for 90 min, then kept B constant at 90% for 5 min, and sharply decreased to 5% B for 5 min for re-equilibration of the column with the constant flow rate set to 400 nl min^{-1}. The data-dependent acquisition method was set as follows: full MS resolution of 120,000; MS1 Automatic Gain Control (AGC) target of 1×10^6; MS1 maximum injection time (IT) of 200 ms; scan range of 300 to 1800; data-dependent tandem MS (MS/MS) resolution of 30,000; MS/MS AGC target of 2×10^5; MS2 maximum IT of 300 ms; fragmentation was enforced by higher-energy collisional dissociation with stepped collision energy with 25, 27, and 30; loop count top of 12; isolation window of 1.5; fixed first mass of 130; MS2 minimum AGC target of 800; charge exclusion: unassigned,1, 2, 3, 8, and >8; peptide match off; exclude isotope on; dynamic exclusion of 45 s. Raw files were converted to mgf format with TurboRawToMGF 2.0.8 (*77*): Precursor mass weight range of 300 to 10,000 Da and all default removal options were off. Searches for cross-linked peptides were performed by MeroX 2.0.0.5 (*78*) with the default setting for DSBU with the following minor modifications: mass limit from 300 to 10,000 Da, minimum charge (MS1) set to 4, apply prescore and score cutoff to 10, and false discovery rate (FDR) cutoff set to 1%. All search results from each fraction's MS acquisition was combined and filtered by recalculated FDR at 1%. Redundant cross-linked pairs were sorted by the main score, and the top hit was chosen for the final report table and mapping onto the structure in Chimera (*73*) with Xlink Analyzer plugin (*79*).

Molecular dynamics simulation

Preparation of the model protein structure began with a cryo-EM structure of yeast CDK8-CycC-Med12N that contained some disconnected outer-loop regions that were remote from our areas of interest. To obtain an intact structure of the complex for molecular dynamics simulation, we used the online homology model builder SWISS-MODEL (*80*) with human CDK8-CycC structure (PDB ID: 5XS2 (*81*)] as a template. For the simulations of mutant Med12N, we used the Swiss PDB Viewer program (*82*) to perform the mutations, which selects the most energetically favorable rotamers of the mutated residue side chains. Molecular dynamics simulations were prepared and carried out by the Amber18 molecular dynamics package (*83*) using the ff14SB force field for proteins (*84*). All systems were solvated with a rectangular box of explicit TIP3P water extending 12 Å beyond the solute edges. Explicit Cl^- ions were added only to neutralize the overall system charge. Systems were minimized in three steps, starting with hydrogen atoms only, then protein side chains, and, lastly, the entire structure, for 500, 5000, and 5000 steps, respectively. This was followed by isothermic-isobaric (NPT) ensemble equilibration in 50-K increments from 100 to 298 K, first for water only and then for the entire system, for 200 ps at each temperature. All production molecular dynamics simulations were performed in the NPT ensemble at 298 K using the Langevin thermostat for 500 ns with a 2-fs time step. A 12-Å cutoff distance was used for direct nonbonded energy calculations, and long-range electrostatics were calculated by the particle mesh Ewald method. The SHAKE algorithm was used to constrain water hydrogen atoms. Raw trajectories were saved every 2 ps and then processed and resaved every 20 ps using Amber's cpptraj (*85*) for analysis.

SUPPLEMENTARY MATERIALS

Supplementary material for this article is available at http://advances.sciencemag.org/cgi/content/full/7/3/eabd4484/DC1

View/request a protocol for this paper from *Bio-protocol*.

REFERENCES AND NOTES

1. B. L. Allen, D. J. Taatjes, The Mediator complex: A central integrator of transcription. *Nat. Rev. Mol. Cell Biol.* **16**, 155–166 (2015).
2. S. Malik, R. G. Roeder, The metazoan Mediator co-activator complex as an integrative hub for transcriptional regulation. *Nat. Rev. Genet.* **11**, 761–772 (2010).
3. K.-L. Tsai, X. Yu, S. Gopalan, T.-C. Chao, Y. Zhang, L. Florens, M. P. Washburn, K. Murakami, R. C. Conaway, J. W. Conaway, F. J. Asturias, Mediator structure and rearrangements required for holoenzyme formation. *Nature* **544**, 196–201 (2017).

4. K. Nozawa, T. R. Schneider, P. Cramer, Core Mediator structure at 3.4 Å extends model of transcription initiation complex. *Nature* **545**, 248–251 (2017).
5. K.-L. Tsai, S. Sato, C. Tomomori-Sato, R. C. Conaway, J. W. Conaway, F. J. Asturias, A conserved Mediator-CDK8 kinase module association regulates Mediator-RNA polymerase II interaction. *Nat. Struct. Mol. Biol.* **20**, 611–619 (2013).
6. M. T. Knuesel, K. D. Meyer, C. Bernecky, D. J. Taatjes, The human CDK8 subcomplex is a molecular switch that controls Mediator coactivator function. *Genes Dev.* **23**, 439–451 (2009).
7. Y. J. Kim, S. Björklund, Y. Li, M. H. Sayre, R. D. Kornberg, A multiprotein mediator of transcriptional activation and its interaction with the C-terminal repeat domain of RNA polymerase II. *Cell* **77**, 599–608 (1994).
8. P. M. Flanagan, R. J. Kelleher III, M. H. Sayre, H. Tschochner, R. D. Kornberg, A mediator required for activation of RNA polymerase II transcription in vitro. *Nature* **350**, 436–438 (1991).
9. H. Elmlund, V. Baraznenok, M. Lindahl, C. O. Samuelsen, P. J. B. Koeck, S. Holmberg, H. Hebert, C. M. Gustafsson, The cyclin-dependent kinase 8 module sterically blocks Mediator interactions with RNA polymerase II. *Proc. Natl. Acad. Sci. U.S.A.* **103**, 15788–15793 (2006).
10. C. O. Samuelsen, V. Baraznenok, O. Khorosjutina, H. Spåhr, T. Kieselbach, S. Holmberg, C. M. Gustafsson, TRAP230/ARC240 and TRAP240/ARC250 Mediator subunits are functionally conserved through evolution. *Proc. Natl. Acad. Sci. U.S.A.* **100**, 6422–6427 (2003).
11. J. Nemet, B. Jelicic, I. Rubelj, M. Sopta, The two faces of Cdk8, a positive/negative regulator of transcription. *Biochimie* **97**, 22–27 (2014).
12. A. J. Donner, C. C. Ebmeier, D. J. Taatjes, J. M. Espinosa, CDK8 is a positive regulator of transcriptional elongation within the serum response network. *Nat. Struct. Mol. Biol.* **17**, 194–201 (2010).
13. C. J. Hengartner, C. M. Thompson, J. Zhang, D. M. Chao, S. M. Liao, A. J. Koleske, S. Okamura, R. A. Young, Association of an activator with an RNA polymerase II holoenzyme. *Genes Dev.* **9**, 897–910 (1995).
14. R. Firestein, A. J. Bass, S. Y. Kim, I. F. Dunn, S. J. Silver, I. Guney, E. Freed, A. H. Ligon, N. Vena, S. Ogino, M. G. Chheda, P. Tamayo, S. Finn, Y. Shrestha, J. S. Boehm, S. Jain, E. Bojarski, C. Mermel, J. Barretina, J. A. Chan, J. Baselga, J. Tabernero, D. E. Root, C. S. Fuchs, M. Loda, R. A. Shivdasani, M. Meyerson, W. C. Hahn, CDK8 is a colorectal cancer oncogene that regulates β-catenin activity. *Nature* **455**, 547–551 (2008).
15. C. J. Hengartner, V. E. Myer, S.-M. Liao, C. J. Wilson, S. S. Koh, R. A. Young, Temporal regulation of RNA polymerase II by Srb10 and Kin28 cyclin-dependent kinases. *Mol. Cell* **2**, 43–53 (1998).
16. S. Akoulitchev, S. Chuikov, D. Reinberg, TFIIH is negatively regulated by cdk8-containing mediator complexes. *Nature* **407**, 102–106 (2000).
17. S.-M. Liao, J. Zhang, D. A. Jeffery, A. J. Koleske, C. M. Thompson, D. M. Chao, M. Viljoen, H. J. J. van Vuuren, R. A. Young, A kinase-cyclin pair in the RNA polymerase II holoenzyme. *Nature* **374**, 193–196 (1995).
18. Z. C. Poss, C. C. Ebmeier, A. T. Odell, A. Tangpeerachaikul, T. Lee, H. E. Pelish, M. D. Shair, R. D. Dowell, W. M. Old, D. J. Taatjes, Identification of Mediator kinase substrates in human cells using Cortistatin A and quantitative phosphoproteomics. *Cell Rep.* **15**, 436–450 (2016).
19. M. Turunen, J. M. Spaeth, S. Keskitalo, M. J. Park, T. Kivioja, A. D. Clark, N. Mäkinen, F. Gao, K. Palin, H. Nurkkala, A. Vähärautio, M. Aavikko, K. Kämpjärvi, P. Vahteristo, C. A. Kim, L. A. Aaltonen, M. Varjosalo, J. Taipale, T. G. Boyer, Uterine leiomyoma-linked MED12 mutations disrupt mediator-associated CDK activity. *Cell Rep.* **7**, 654–660 (2014).
20. M. J. Park, H. Shen, J. M. Spaeth, J. H. Tolvanen, C. Failor, J. F. Knudtson, J. McLaughlin, S. K. Halder, Q. Yang, S. E. Bulun, A. Al-Hendy, R. S. Schenken, L. A. Aaltonen, T. G. Boyer, Oncogenic exon 2 mutations in Mediator subunit MED12 disrupt allosteric activation of cyclin C-CDK8/19. *J. Biol. Chem.* **293**, 4870–4882 (2018).
21. M. T. Knuesel, K. D. Meyer, A. J. Donner, J. M. Espinosa, D. J. Taatjes, The human CDK8 subcomplex is a histone kinase that requires Med12 for activity and can function independently of Mediator. *Mol. Cell. Biol.* **29**, 650–661 (2009).
22. F. Lai, U. A. Orom, M. Cesaroni, M. Beringer, D. J. Taatjes, G. A. Blobel, R. Shiekhattar, Activating RNAs associate with Mediator to enhance chromatin architecture and transcription. *Nature* **494**, 497–501 (2013).
23. S. Kim, X. Xu, A. Hecht, T. G. Boyer, Mediator is a transducer of Wnt/β-catenin signaling. *J. Biol. Chem.* **281**, 14066–14075 (2006).
24. R. Zhou, N. Bonneaud, C.-X. Yuan, P. de Santa Barbara, B. Boizet, S. Tibor, G. Scherer, R. G. Roeder, F. Poulat, P. Berta, SOX9 interacts with a component of the human thyroid hormone receptor-associated protein complex. *Nucleic Acids Res.* **30**, 3245–3252 (2002).
25. D. Cheng, V. Vemulapalli, Y. Lu, J. Shen, S. Aoyagi, C. J. Fry, Y. Yang, C. E. Foulds, F. Stossi, L. S. Treviño, M. A. Mancini, B. W. O'Malley, C. L. Walker, T. G. Boyer, M. T. Bedford, CARM1 methylates MED12 to regulate its RNA-binding ability. *Life Sci. Alliance* **1**, e201800117 (2018).
26. N. Ding, H. Zhou, P.-O. Esteve, H. G. Chin, S. Kim, X. Xu, S. M. Joseph, M. J. Friez, C. E. Schwartz, S. Pradhan, T. G. Boyer, Mediator links epigenetic silencing of neuronal gene expression with X-linked mental retardation. *Mol. Cell* **31**, 347–359 (2008).
27. A. M. Burroughs, L. M. Iyer, L. Aravind, Two novel PIWI families: Roles in inter-genomic conflicts in bacteria and Mediator-dependent modulation of transcription in eukaryotes. *Biol. Direct* **8**, 13 (2013).
28. D. C. Swarts, K. Makarova, Y. Wang, K. Nakanishi, R. F. Ketting, E. V. Koonin, D. J. Patel, J. van der Oost, The evolutionary journey of Argonaute proteins. *Nat. Struct. Mol. Biol.* **21**, 743–753 (2014).
29. N. T. Schirle, J. Sheu-Gruttadauria, I. J. MacRae, Structural basis for microRNA targeting. *Science* **346**, 608–613 (2014).
30. Y. Wang, G. Sheng, S. Juranek, T. Tuschl, D. J. Patel, Structure of the guide-strand-containing argonaute silencing complex. *Nature* **456**, 209–213 (2008).
31. A. T. Vulto-van Silfhout, B. B. A. de Vries, B. W. M. van Bon, A. Hoischen, M. Ruiterkamp-Versteeg, C. Gilissen, F. Gao, M. van Zwam, C. L. Harteveld, A. J. van Essen, B. C. J. Hamel, T. Kleefstra, M. A. A. P. Willemsen, H. G. Yntema, H. van Bokhoven, H. G. Brunner, T. G. Boyer, A. P. M. de Brouwer, Mutations in MED12 cause X-linked Ohdo syndrome. *Am. J. Hum. Genet.* **92**, 401–406 (2013).
32. H.-R. Heinonen, A. Pasanen, O. Heikinheimo, T. Tanskanen, K. Palin, J. Tolvanen, P. Vahteristo, J. Sjöberg, E. Pitkänen, R. Bützow, N. Mäkinen, L. A. Aaltonen, Multiple clinical characteristics separate MED12-mutation-positive and -negative uterine leiomyomas. *Sci. Rep.* **7**, 1015 (2017).
33. H. Risheg, J. M. Graham Jr., R. D. Clark, R. C. Rogers, J. M. Opitz, J. B. Moeschler, A. P. Peiffer, M. May, S. M. Joseph, J. R. Jones, R. E. Stevenson, C. E. Schwartz, M. J. Friez, A recurrent mutation in MED12 leading to R961W causes Opitz-Kaveggia syndrome. *Nat. Genet.* **39**, 451–453 (2007).
34. C. E. Schwartz, P. S. Tarpey, H. A. Lubs, A. Verloes, M. M. May, H. Risheg, M. J. Friez, P. A. Futreal, S. Edkins, J. Teague, S. Briault, C. Skinner, A. Bauer-Carlin, R. J. Simensen, S. M. Joseph, J. R. Jones, J. Gecz, M. R. Stratton, F. L. Raymond, R. E. Stevenson, The original Lujan syndrome family has a novel missense mutation (p.N1007S) in the MED12 gene. *J. Med. Genet.* **44**, 472–477 (2007).
35. K. Kämpjärvi, N. H. Kim, S. Keskitalo, A. D. Clark, P. von Nandelstadh, M. Turunen, T. Heikkinen, M. J. Park, N. Mäkinen, K. Kivinummi, S. Lintula, K. Hotakainen, H. Nevanlinna, P. Hokland, T. Böhling, R. Bützow, J. Böhm, J.-P. Mecklin, H. Järvinen, M. Kontro, T. Visakorpi, J. Taipale, M. Varjosalo, T. G. Boyer, P. Vahteristo, Somatic MED12 mutations in prostate cancer and uterine leiomyomas promote tumorigenesis through distinct mechanisms. *Prostate* **76**, 22–31 (2016).
36. X. Wang, J. Wang, Z. Ding, J. Ji, Q. Sun, G. Cai, Structural flexibility and functional interaction of Mediator Cdk8 module. *Protein Cell* **4**, 911–920 (2013).
37. S. Hoeppner, S. Baumli, P. Cramer, Structure of the Mediator subunit cyclin C and its implications for CDK8 function. *J. Mol. Biol.* **350**, 833–842 (2005).
38. E. V. Schneider, J. Böttcher, M. Blaesse, L. Neumann, R. Huber, K. Maskos, The structure of CDK8/CycC implicates specificity in the CDK/cyclin family and reveals interaction with a deep pocket binder. *J. Mol. Biol.* **412**, 251–266 (2011).
39. D. J. Wood, J. A. Endicott, Structural insights into the functional diversity of the CDK-cyclin family. *Open Biol.* **8**, 180112 (2018).
40. A. A. Russo, P. D. Jeffrey, N. P. Pavletich, Structural basis of cyclin-dependent kinase activation by phosphorylation. *Nat. Struct. Biol.* **3**, 696–700 (1996).
41. U. Schulze-Gahmen, S.-H. Kim, Structural basis for CDK6 activation by a virus-encoded cyclin. *Nat. Struct. Biol.* **9**, 177–181 (2002).
42. M. J. Park, H. Shen, N. H. Kim, F. Gao, C. Failor, J. F. Knudtson, J. McLaughlin, S. K. Halder, T. A. Heikkinen, P. Vahteristo, A. Al-Hendy, R. S. Schenken, T. G. Boyer, Mediator kinase disruption in MED12-mutant uterine fibroids from Hispanic women of South Texas. *J. Clin. Endocrinol. Metab.* **103**, 4283–4292 (2018).
43. K. Kämpjärvi, T. M. Järvinen, T. Heikkinen, A. S. Ruppert, L. Senter, K. W. Hoag, O. Dufva, M. Kontro, L. Rassenti, E. Hertlein, T. J. Kipps, K. Porkka, J. C. Byrd, A. de la Chapelle, P. Vahteristo, Somatic MED12 mutations are associated with poor prognosis markers in chronic lymphocytic leukemia. *Oncotarget* **6**, 1884–1888 (2015).
44. G. Meister, Argonaute proteins: Functional insights and emerging roles. *Nat. Rev. Genet.* **14**, 447–459 (2013).
45. K. Nakanishi, Anatomy of RISC: How do small RNAs and chaperones activate Argonaute proteins? *Wiley Interdiscip. Rev. RNA* **7**, 637–660 (2016).
46. K. Nakanishi, D. E. Weinberg, D. P. Bartel, D. J. Patel, Structure of yeast Argonaute with guide RNA. *Nature* **486**, 368–374 (2012).
47. N. T. Schirle, I. J. MacRae, The crystal structure of human Argonaute2. *Science* **336**, 1037–1040 (2012).
48. E. Elkayam, C.-D. Kuhn, A. Tocilj, A. D. Haase, E. M. Greene, G. J. Hannon, L. Joshua-Tor, The structure of human argonaute-2 in complex with miR-20a. *Cell* **150**, 100–110 (2012).
49. K. Nakanishi, M. Ascano, T. Gogakos, S. Ishibe-Murakami, A. A. Serganov, D. Briskin, P. Morozov, T. Tuschl, D. J. Patel, Eukaryote-specific insertion elements control human ARGONAUTE slicer activity. *Cell Rep.* **3**, 1893–1900 (2013).
50. C. R. Faehnle, E. Elkayam, A. D. Haase, G. J. Hannon, L. Joshua-Tor, The making of a slicer: Activation of human Argonaute-1. *Cell Rep.* **3**, 1901–1909 (2013).

51. M. S. Park, H.-D. Phan, F. Busch, S. H. Hinckley, J. A. Brackbill, V. H. Wysocki, K. Nakanishi, Human Argonaute3 has slicer activity. *Nucleic Acids Res.* **45**, 11867–11877 (2017).
52. M. S. Park, R. Araya-Secchi, J. A. Brackbill, H.-D. Phan, A. C. Kehling, E. W. Abd El-Wahab, D. M. Dayeh, M. Sotomayor, K. Nakanishi, Multidomain convergence of Argonaute during RISC assembly correlates with the formation of internal water clusters. *Mol. Cell* **75**, 725–740.e6 (2019).
53. F. Klatt, A. Leitner, I. V. Kim, H. Ho-Xuan, E. V. Schneider, F. Langhammer, R. Weinmann, M. R. Müller, R. Huber, G. Meister, C.-D. Kuhn, A precisely positioned MED12 activation helix stimulates CDK8 kinase activity. *Proc. Natl. Acad. Sci. U.S.A.* **117**, 2894–2905 (2020).
54. A. D. Clark, M. Oldenbroek, T. G. Boyer, Mediator kinase module and human tumorigenesis. *Crit. Rev. Biochem. Mol. Biol.* **50**, 393–426 (2015).
55. W. K. Lim, C. K. Ong, J. Tan, A. A. Thike, C. C. Y. Ng, V. Rajasegaran, S. S. Myint, S. Nagarajan, N. D. M. Nasir, J. R. McPherson, I. Cutcutache, G. Poore, S. T. Tay, W. S. Ooi, V. K. M. Tan, M. Hartman, K. W. Ong, B. K. T. Tan, S. G. Rozen, P. H. Tan, P. Tan, B. T. Teh, Exome sequencing identifies highly recurrent MED12 somatic mutations in breast fibroadenoma. *Nat. Genet.* **46**, 877–880 (2014).
56. I. Menzl, T. Zhang, A. Berger-Becvar, R. Grausenburger, G. Heller, M. Prchal-Murphy, L. Edlinger, V. M. Knab, I. Z. Uras, E. Grundschober, K. Bauer, M. Roth, A. Skucha, Y. Liu, J. M. Hatcher, Y. Liang, N. P. Kwiatkowski, D. Fux, A. Hoelbl-Kovacic, S. Kubicek, J. V. Melo, P. Valent, T. Weichhart, F. Grebien, J. Zuber, N. S. Gray, V. Sexl, A kinase-independent role for CDK8 in BCR-ABL1$^+$ leukemia. *Nat. Commun.* **10**, 4741 (2019).
57. Y. Zhu, C. M. Schluttenhoffer, P. Wang, F. Fu, J. Thimmapuram, J.-K. Zhu, S. Y. Lee, D.-J. Yun, T. Mengiste, CYCLIN-DEPENDENT KINASE8 differentially regulates plant immunity to fungal pathogens through kinase-dependent and -independent functions in Arabidopsis. *Plant Cell* **26**, 4149–4170 (2014).
58. Y.-R. Yuan, Y. Pei, J.-B. Ma, V. Kuryavyi, M. Zhadina, G. Meister, H.-Y. Chen, Z. Dauter, T. Tuschl, D. J. Patel, Crystal structure of *A. aeolicus* argonaute, a site-specific DNA-guided endoribonuclease, provides insights into RISC-mediated mRNA cleavage. *Mol. Cell* **19**, 405–419 (2005).
59. F. V. Rivas, N. H. Tolia, J.-J. Song, J. P. Aragon, J. Liu, G. J. Hannon, L. Joshua-Tor, Purified Argonaute2 and an siRNA form recombinant human RISC. *Nat. Struct. Mol. Biol.* **12**, 340–349 (2005).
60. S. Willkomm, C. A. Oellig, A. Zander, T. Restle, R. Keegan, D. Grohmann, S. Schneider, Structural and mechanistic insights into an archaeal DNA-guided Argonaute protein. *Nat. Microbiol.* **2**, 17035 (2017).
61. X. Zhu, M. Wirén, I. Sinha, N. N. Rasmussen, T. Linder, S. Holmberg, K. Ekwall, C. M. Gustafsson, Genome-wide occupancy profile of Mediator and the Srb8-11 module reveals interactions with coding regions. *Mol. Cell* **22**, 169–178 (2006).
62. J.-C. Andrau, L. van de Pasch, P. Lijnzaad, T. Bijma, M. G. Koerkamp, J. van de Peppel, M. Werner, F. C. P. Holstege, Genome-wide location of the coactivator mediator: Binding without activation and transient Cdk8 interaction on DNA. *Mol. Cell* **22**, 179–192 (2006).
63. L. Wahba, J. D. Amon, D. Koshland, M. Vuica-Ross, RNase H and multiple RNA biogenesis factors cooperate to prevent RNA:DNA hybrids from generating genome instability. *Mol. Cell* **44**, 978–988 (2011).
64. H. E. Pelish, B. B. Liau, I. I. Nitulescu, A. Tangpeerachaikul, Z. C. Poss, D. H. Da Silva, B. T. Caruso, A. Arefolov, O. Fadeyi, A. L. Christie, K. Du, D. Banka, E. V. Schneider, A. Jestel, G. Zou, C. Si, C. C. Ebmeier, R. T. Bronson, A. V. Krivtsov, A. G. Myers, N. E. Kohl, A. L. Kung, S. A. Armstrong, M. E. Lemieux, D. J. Taatjes, M. D. Shair, Mediator kinase inhibition further activates super-enhancer-associated genes in AML. *Nature* **526**, 273–276 (2015).
65. S. Schilbach, M. Hantsche, D. Tegunov, C. Dienemann, C. Wigge, H. Urlaub, P. Cramer, Structures of transcription pre-initiation complex with TFIIH and Mediator. *Nature* **551**, 204–209 (2017).
66. O. Puig, F. Caspary, G. Rigaut, B. Rutz, E. Bouveret, E. Bragado-Nilsson, M. Wilm, B. Séraphin, The tandem affinity purification (TAP) method: A general procedure of protein complex purification. *Methods* **24**, 218–229 (2001).
67. S. Q. Zheng, E. Palovcak, J.-P. Armache, K. A. Verba, Y. Cheng, D. A. Agard, MotionCor2: Anisotropic correction of beam-induced motion for improved cryo-electron microscopy. *Nat. Methods* **14**, 331–332 (2017).
68. K. Zhang, Gctf: Real-time CTF determination and correction. *J. Struct. Biol.* **193**, 1–12 (2016).
69. S. H. W. Scheres, RELION: Implementation of a Bayesian approach to cryo-EM structure determination. *J. Struct. Biol.* **180**, 519–530 (2012).
70. K. Zhang (2017); www.mrc-lmb.cam.ac.uk/kzhang/.
71. A. Punjani, J. L. Rubinstein, D. J. Fleet, M. A. Brubaker, cryoSPARC: Algorithms for rapid unsupervised cryo-EM structure determination. *Nat. Methods* **14**, 290–296 (2017).
72. R. Henderson, A. Sali, M. L. Baker, B. Carragher, B. Devkota, K. H. Downing, E. H. Egelman, Z. Feng, J. Frank, N. Grigorieff, W. Jiang, S. J. Ludtke, O. Medalia, P. A. Penczek, P. B. Rosenthal, M. G. Rossmann, M. F. Schmid, G. F. Schröder, A. C. Steven, D. L. Stokes, J. D. Westbrook, W. Wriggers, H. Yang, J. Young, H. M. Berman, W. Chiu, G. J. Kleywegt, C. L. Lawson, Outcome of the first electron microscopy validation task force meeting. *Structure* **20**, 205–214 (2012).
73. E. F. Pettersen, T. D. Goddard, C. C. Huang, G. S. Couch, D. M. Greenblatt, E. C. Meng, T. E. Ferrin, UCSF Chimera—A visualization system for exploratory research and analysis. *J. Comput. Chem.* **25**, 1605–1612 (2004).
74. L. A. Kelley, S. Mezulis, C. M. Yates, M. N. Wass, M. J. E. Sternberg, The Phyre2 web portal for protein modeling, prediction and analysis. *Nat. Protoc.* **10**, 845–858 (2015).
75. P. Emsley, B. Lohkamp, W. G. Scott, K. Cowtan, Features and development of Coot. *Acta Crystallogr. D Biol. Crystallogr.* **66**, 486–501 (2010).
76. P. D. Adams, P. V. Afonine, G. Bunkóczi, V. B. Chen, I. W. Davis, N. Echols, J. J. Headd, L.-W. Hung, G. J. Kapral, R. W. Grosse-Kunstleve, A. J. McCoy, N. W. Moriarty, R. Oeffner, R. J. Read, D. C. Richardson, J. S. Richardson, T. C. Terwilliger, P. H. Zwart, PHENIX: A comprehensive Python-based system for macromolecular structure solution. *Acta Crystallogr. D Biol. Crystallogr.* **66**, 213–221 (2010).
77. Q. Sheng, R. Li, J. Dai, Q. Li, Z. Su, Y. Guo, C. Li, Y. Shyr, R. Zeng, Preprocessing significantly improves the peptide/protein identification sensitivity of high-resolution isobarically labeled tandem mass spectrometry data. *Mol. Cell. Proteomics* **14**, 405–417 (2015).
78. C. Iacobucci, M. Götze, C. H. Ihling, C. Piotrowski, C. Arlt, M. Schäfer, C. Hage, R. Schmidt, A. Sinz, A cross-linking/mass spectrometry workflow based on MS-cleavable cross-linkers and the MeroX software for studying protein structures and protein-protein interactions. *Nat. Protoc.* **13**, 2864–2889 (2018).
79. J. Kosinski, A. von Appen, A. Ori, K. Karius, C. W. Müller, M. Beck, Xlink Analyzer: Software for analysis and visualization of cross-linking data in the context of three-dimensional structures. *J. Struct. Biol.* **189**, 177–183 (2015).
80. A. Waterhouse, M. Bertoni, S. Bienert, G. Studer, G. Tauriello, R. Gumienny, F. T. Heer, T. A. P. de Beer, C. Rempfer, L. Bordoli, R. Lepore, T. Schwede, SWISS-MODEL: Homology modelling of protein structures and complexes. *Nucleic Acids Res.* **46**, W296–W303 (2018).
81. X. Han, M. Jiang, C. Zhou, Z. Zhou, Z. Xu, L. Wang, A. V. Mayweg, R. Niu, T.-G. Jin, S. Yang, Discovery of potent and selective CDK8 inhibitors through FBDD approach. *Bioorg. Med. Chem. Lett.* **27**, 4488–4492 (2017).
82. N. Guex, M. C. Peitsch, T. Schwede, Automated comparative protein structure modeling with SWISS-MODEL and Swiss-PdbViewer: A historical perspective. *Electrophoresis* **30** (suppl. 1), S162–S173 (2009).
83. I. Y. B.-S. D. A. Case, S. R. Brozell, D. S. Cerutti, T. E. Cheatham III, V. W. D. Cruzeiro, T. A. Darden, R. E. Duke, D. Ghoreishi, M. K. Gilson, H. Gohlke, A. W. Goetz, D. Greene, R. Harris, N. Homeyer, Y. Huang, S. Izadi, A. Kovalenko, T. Kurtzman, T. S. Lee, S. LeGrand, P. Li, C. Lin, J. Liu, T. Luchko, R. Luo, D. J. Mermelstein, K. M. Merz, Y. Miao, G. Monard, C. Nguyen, H. Nguyen, I. Omelyan, A. Onufriev, F. Pan, R. Qi, D. R. Roe, A. Roitberg, C. Sagui, S. Schott-Verdugo, J. Shen, C. L. Simmerling, J. Smith, R. Salomon- Ferrer, J. Swails, R. C. Walker, J. Wang, H. Wei, R. M. Wolf, X. Wu, L. Xiao, D. M. York, P. A. Kollman, *AMBER 2018* (University of California, San Francisco, 2018).
84. J. A. Maier, C. Martinez, K. Kasavajhala, L. Wickstrom, K. E. Hauser, C. Simmerling, ff14SB: Improving the accuracy of protein side chain and backbone parameters from ff99SB. *J. Chem. Theory Comput.* **11**, 3696–3713 (2015).
85. D. R. Roe, T. E. Cheatham III, PTRAJ and CPPTRAJ: Software for processing and analysis of molecular dynamics trajectory data. *J. Chem. Theory Comput.* **9**, 3084–3095 (2013).
86. E. V. Schneider, J. Böttcher, R. Huber, K. Maskos, L. Neumann, Structure-kinetic relationship study of CDK8/CycC specific compounds. *Proc. Natl. Acad. Sci. U.S.A.* **110**, 8081–8086 (2013).
87. T. Dale, P. A. Clarke, C. Esdar, D. Waalboer, O. Adeniji-Popoola, M.-J. Ortiz-Ruiz, A. Mallinger, R. S. Samant, P. Czodrowski, D. Musil, D. Schwarz, K. Schneider, M. Stubbs, K. Ewan, E. Fraser, R. TePoele, W. Court, G. Box, M. Valenti, A. de Haven Brandon, S. Gowan, F. Rohdich, F. Raynaud, R. Schneider, O. Poeschke, A. Blaukat, P. Workman, K. Schiemann, S. A. Eccles, D. Wienke, J. Blagg, A selective chemical probe for exploring the role of CDK8 and CDK19 in human disease. *Nat. Chem. Biol.* **11**, 973–980 (2015).
88. P. Czodrowski, A. Mallinger, D. Wienke, C. Esdar, O. Pöschke, M. Busch, F. Rohdich, S. A. Eccles, M.-J. Ortiz-Ruiz, R. Schneider, F. I. Raynaud, P. A. Clarke, D. Musil, D. Schwarz, T. Dale, K. Urbahns, J. Blagg, K. Schiemann, Structure-based optimization of potent, selective, and orally bioavailable CDK8 inhibitors discovered by high-throughput screening. *J. Med. Chem.* **59**, 9337–9349 (2016).
89. P. Bergeron, M. F. T. Koehler, E. M. Blackwood, K. Bowman, K. Clark, R. Firestein, J. R. Kiefer, K. Maskos, M. L. McCleland, L. Orren, S. Ramaswamy, L. Salphati, S. Schmidt, E. V. Schneider, J. Wu, M. Beresini, Design and development of a series of potent and selective type II inhibitors of CDK8. *ACS Med. Chem. Lett.* **7**, 595–600 (2016).
90. A. Mallinger, K. Schiemann, C. Rink, F. Stieber, M. Calderini, S. Crumpler, M. Stubbs, O. Adeniji-Popoola, O. Poeschke, M. Busch, P. Czodrowski, D. Musil, D. Schwarz, M.-J. Ortiz-Ruiz, R. Schneider, C. Thai, M. Valenti, A. de Haven Brandon, R. Burke, P. Workman, T. Dale, D. Wienke, P. A. Clarke, C. Esdar, F. I. Raynaud, S. A. Eccles, F. Rohdich, J. Blagg, Discovery of potent, selective, and orally bioavailable small-molecule modulators of the mediator complex-associated kinases CDK8 and CDK19. *J. Med. Chem.* **59**, 1078–1101 (2016).

Acknowledgments: We thank F. Asturias for helpful discussions and critical reading of the manuscript. We thank K. Morano, N. Kim, and P. Christie for providing a Med13Δ yeast strain, a yeast pNK150 plasmid, and two *E. coli* expression plasmids, respectively. We thank T. Otomo for providing a TEV protease expression plasmid. We thank the Electron Cryo-Microscopy Core Facility of the UTHealth McGovern Medical School for cryo-EM data collection. We thank MS facilities at the University of Pennsylvania and the UTHealth for the XL-MS analysis and protein identification, respectively. **Funding:** This work was supported by the Cancer Prevention Research Institute of Texas, grant number 13127 to CPRIT Scholar in Cancer Research, K.-L.T., and the Welch Foundation (AU-2050-20200401) and U.S. National Institutes of Health grants CA196539, GM110174, and AI118891 (B.A.G.), HD087417 and HD094378 (T.G.B.), R01 GM124320 (K.N.), R01 GM123233 (K.M.), R01 GM-109045 (C.-e.C.), and S10 OD023592-01 and T32 GM133398-01 (H.J.K.). Y.-C.L. was supported, in part, by the Ministry of Science and Technology, Taiwan, R.O.C. under grant number MOST 108-2917-I-564-025. **Author contributions:** Y.-C.L., T.-C.C., and K.-L.T. performed all experiments related to high-resolution cryo-EM analysis, including cryo-EM grid preparation, cryo-EM data collection and processing, and model building and refinement. Y.-C.L., T.-C.C., G.L., S.-F.C., and L.S. executed yeast cell culture and CKM purification. H.J.K., K.M., and B.A.G. designed and performed XL-MS analysis of the CKM. Y.-C.L. and T.-C.C. performed expression and purification of recombinant Med12 proteins. T.C. and C.-e.C. performed molecular dynamics simulation experiments. Y.-C.L., T.-C.C., and T.G.B. designed and performed binding assay and kinase activity measurement. Y.-C.L., T.-C.C., H.J.K., T.C., C.-e.C., K.N., K.M., B.A.G., T.G.B., and K.-L.T. discussed, interpreted results, and wrote the manuscript. **Competing interests:** The authors declare that they have no competing interests. **Data and materials availability:** Cryo-EM maps of the yeast CKM, Kinase/Central-lobes, and H-lobe were deposited to the EMDataBank with accession numbers EMD-22991, EMD-22989, and EMD-22990, respectively. Their corresponding atomic models were deposited to the RCSB Protein Data Bank with accession numbers 7KPX, 7KPV, and 7KPW, respectively. All data needed to evaluate the conclusions in the paper are present in the paper and/or the Supplementary Materials. Additional data related to this paper may be requested from the authors.

Submitted 22 June 2020
Accepted 25 November 2020
Published 15 January 2021
10.1126/sciadv.abd4484

Citation: Y.-C. Li, T.-C. Chao, H. J. Kim, T. Cholko, S.-F. Chen, G. Li, L. Snyder, K. Nakanishi, C.-e. Chang, K. Murakami, B. A. Garcia, T. G. Boyer, K.-L. Tsai, Structure and noncanonical Cdk8 activation mechanism within an Argonaute-containing Mediator kinase module. *Sci. Adv.* **7**, eabd4484 (2021).